THESIS FOR THE DEGREE OF LICENTIATE OF ENGINEERING

Cr Vaporization and Oxide Scale Growth on Interconnects in Solid Oxide Fuel Cells

Hannes Falk Windisch

Department of Chemistry and Chemical Engineering

CHALMERS UNIVERSITY OF TECHNOLOGY

Gothenburg, Sweden 2015

Cr Vaporization and Oxide Scale Growth on Interconnects in Solid Oxide Fuel Cells

Hannes Falk Windisch

Department of Chemistry and Chemical Engineering

Chalmers University of Technology

SE-412 96 Gothenburg

Sweden

Telephone + 46 (0)31-772 2850

Cover:

SEM image and EDX elemental maps from a thin lamella of the mechanically deformed steel Crofer 22 APU coated with 600 nm Co (pre-coated) after 24 h of exposure in air-3% H2O at 850 °C.

Cr Vaporization and Oxide Scale Growth on Interconnects in Solid Oxide Fuel Cells

Hannes Falk Windisch

Department of Chemistry and Chemical Engineering

Chalmers University of Technology

Abstract

The vaporization of Cr(VI) species and the greater electrical resistance caused by a growing oxide scale are probably the two most detrimental degradation mechanisms associated with the use of Cr_2O_3-forming alloys as the interconnect material in a Solid Oxide Fuel Cell (SOFC). High electrical efficiency, clean emissions and the possibility to utilize several types of fuels, such as hydrogen, alcohols and hydrocarbons are some of the great advantages of SOFC technology. However, the limited lifetime and high production costs of a SOFC have limited the commercialization of this technology. Therefore, improving the component materials and reducing production costs is of great importance. This thesis has examined both mechanisms; Cr vaporization and oxide scale growth. The possibility to pre-coat large amounts of steel and deform the material to allow for gas distribution as an alternative method for reducing production costs was also investigated. To achieve these objectives, nano coatings of Co and Ce were applied to Cr_2O_3-forming ferritic stainless steels to decrease Cr vaporization and improve the oxidation resistance of the interconnect material. All exposures were carried out in a simulated cathode-side environment consisting of air-3% H_2O. Cr vaporization was measured using a denuder technique and oxide-scale growth was studied mainly gravimetrically. For chemical, structural and microstructural analysis, SEM/EDX, FIB and XRD techniques were used.

The results presented in this thesis show that high quality coatings that mitigate Cr vaporization are necessary, even if the SOFC operating temperature is decreased to temperatures as low as 650 ºC. By coating a ferritic stainless steel with 600 nm Co, the Cr vaporization rate can be decreased by almost 90 %, and by adding an extra 10 nm layer of Ce, the high temperature corrosion resistance of the interconnect material can be significantly improved, and electrical oxide-scale resistance can be reduced. When the pre-coated steel was mechanically deformed to allow for gas distribution, large cracks formed in the coating. However, upon exposure, the cracks healed and formed a continuous surface oxide rich in Co and Mn. As an effect of this rapid healing, no increase in Cr vaporization was detected for the pre-coated material.

Keywords: SOFC, Interconnect, Corrosion, Cr Vaporization, Coatings

List of Publications

The thesis is based primarily on the following three papers:

Paper I

Hannes Falk-Windisch, Jan Erik Svensson and Jan Froitzheim

The Effect of Temperature on Chromium Vaporization and Oxide Scale Growth on Interconnect Steels for Solid Oxide Fuel Cells, Journal of Power Sources, Volume 287, 7 April 2015, Pages 25-35, doi:10.1016/j.jpowsour.2015.04.040

Paper II

Hannes Falk-Windisch, Mohammad Sattari, Jan-Erik Svensson and Jan Froitzheim

Chromium vaporization from mechanically deformed pre-coated interconnects in Solid Oxide Fuel Cells

Manuscript

Paper III

Anna Magraso; Hannes Falk-Windisch; Jan Froitzheim; Jan-Erik Svensson; Reidar Haugsrud

Reduced long term electrical resistance in Ce/Co-coated ferritic stainless steel for solid oxide fuel cell metallic interconnects

Accepted, Journal of Hydrogen Energy (2015)

Statement of author´s contribution

In paper I and II, I was the main author. Most of the experimental work was carried out by me; the rest was carried out by students under my supervision. All analytical characterization in paper I and II was carried out by me except FIB preparation and SEM/EDX analysis of a thin lamella (Paper II) which was carried out by Mohammad Sattari. In paper III, I was involved in writing the paper and carried out all pre-oxidation exposures that were electrically characterized by the main author Anna Magraso.

Table of Contents

Acknowledgements

1. Introduction

One of society's greatest challenges is the need to simultaneously meet the rapidly increasing demand for energy while reducing the emissions of greenhouse gases.

Fuel cells have emerged as a promising technology for the decentralized production of clean electricity. Fuel cells generate electricity by converting chemical energy stored in the fuel through a chemical reaction. Because of this, they are not limited to the Carnot cycle and, therefore, are able to reach higher electrical efficiencies than combustion engines [1]. The most common type of fuel cell today is the Proton Exchange Membrane Fuel Cell (PEMFC). This type of fuel cell; however, can only operate on hydrogen and needs platinum as a catalyst [2, 3]. The Solid Oxide Fuel Cell (SOFC), in contrast, operates at high temperatures (600 – 800 °C),thus, enabling the possibility to use not only hydrogen as a fuel, but also conventional fuels, such as biogas, natural gas, ethanol and even diesel, without need for platinum [4-7]. All fuel cells consist of three components: an anode, a cathode and an electrolyte. To design a fuel cell system with the desired voltage, several cells must be connected in series to form a fuel cell stack. Each cell in the stack is separated and electrically connected by means of an interconnect.

The interconnect material in an SOFC must fulfil several requirements such as have a Thermal Expansion Coefficient (TEC) similar to the other ceramic parts in the cell, be gas tight, and have high electrical conductivity as well as low contact resistance with the electrodes. It must also be stable in both high pO_2 (the air on the cathode side) and in low pO_2 (the fuel on the anode side) environments, and it must be inexpensive to manufacture [8, 9]. Ferritic Cr_2O_3-forming stainless steels have become the most popular choice for interconnect materials in SOFCs today. However, the vaporization of Cr(VI) species and oxide-scale growth are two detrimental degradation mechanisms in an SOFC associated with the Cr_2O_3-forming interconnect material [8]. During long-term operation, several µm-thick oxide scales are formed at the interconnect surface giving rise to a significant increase in electrical resistance, and, as a consequence, lower electrical output. Furthermore, Cr present at the interconnect surface forms volatile Cr(VI) species on the cathode side [10-13]. These volatile Cr(VI) species are transported to the cathode-gas-electrolyte interface and form a deposit that blocks the electrochemical oxygen reduction process [14-17]. For this reason, ferritic stainless steels are coated with either metallic or ceramic coatings to reduce the vaporization of Cr. The coating material should not increase the electrical resistance of the interconnect material; therefore, spinel- and perovskite-type coatings have been suggested as the most promising coating candidates. Today, the probably most frequently used coating system is the $(Mn,Co)_3O_4$ (MCO) coating. Such a coating can be applied using a variety of different techniques such as spray drying, dip-coating, screen printing, aerosol spray deposition, plasma spraying or with Physical Vapour Deposition (PVD) [18-24]. Another alternative is to coat the steel with metallic Co using PVD or electroplating [25-27]. In such a case, Co_3O_4 will be rapidly formed due to the oxidation of the coating when the SOFC is heated up in air. If the steel contains Mn, Co_3O_4 can turn into $(Mn,Co)_3O_4$ due to the outwards diffusion of Mn from the steel. It has been demonstrated that Co coatings less than 1 µm thick can effectively suppress Cr vaporization

[25, 28, 29]. Furthermore, corrosion resistance can also be improved by applying an additional layer of a reactive element such as Ce or La [29, 30].

For SOFC technology to become economically attractive, the cost must be reduced significantly. Today, most coated interconnect materials are manufactured in two separate steps; (i) stamping the uncoated steel into the shape of the interconnect to allow for gas distribution, followed by (ii) coating the deformed steel plate in a second step. This two-step batch-coating concept is rather inefficient for mass production. By applying thin metallic coatings, large amounts of steel can be pre-coated and shaped into interconnects that allow for much more efficient large-scale production, and lower overall cost.

1.1 Aim of this thesis

The aim of this thesis is to better understand the two most important degradation mechanisms associated with ferritic stainless steels as the interconnect material in an SOFC, and how thin metallic coatings can be used to address these problems in a cost-effective way.

Due to the very long lifetime of an SOFC, accelerated tests must be developed to study the component materials. The most commonly used method to accelerate corrosion is to expose the material at a higher temperature than the normal operating temperature. However, Cr vaporization and oxide scale growth are two separate degradation mechanisms. Therefore, the aim of Paper I is to study the influence of temperature on both mechanisms.

To reduce Cr vaporization, ferritic stainless steels can be coated with thin Co coatings. Large amounts of steel can be pre-coated and shaped into interconnects. This would allow for efficient large-scale production, and could significantly decrease the overall costs of the interconnect material. However, large cracks can form within the coating due to the mechanical deformation process. The aim of Paper II is to investigate if deformation increases Cr vaporization.

Earlier investigations have shown that thin films of the reactive element Ce could significantly increase the corrosion resistance of ferritic stainless steels. Improved corrosion resistance is only beneficial in an SOFC if it does not increase electrical resistance. For this reason, the aim of Paper III is to investigate if Ce/Co coatings can improve the electrical properties of the interconnect material.

2. Fuel Cells

Fuel cells are devices that can generate electricity (and heat) by converting chemical energy stored in the fuel through a chemical reaction without combustion. They are not limited to Carnot efficiency, and have, therefore, the ability to reach higher electrical efficiencies than combustion engines [1]. They can also generate electricity as long as fuel is available, and they do not need to be recharged like batteries. These properties make fuel cells highly attractive for most electrical applications ranging from small portable devices to large MW power plants.

Each cell is composed of two electrodes (an anode and a cathode) separated by an electrolyte. Similar to batteries, the principle of a fuel cell is to force electrons through an external circuit by utilizing an electrolyte material which is permeable to ions but not to electrons. When the cathode and the anode are electrically connected via an external circuit, ion diffusion through the electrolyte will take place driven by the concentration gradient. To maintain charge balance, electrons give rise to a current in the external circuit [1].

Since the type of electrode material determines which type of ions can diffuse across the electrolyte, a large variation of fuel cell types exist. These are generally classified according to the electrolyte material. Figure 2.1 illustrates the working principle of the most common fuel cell types.
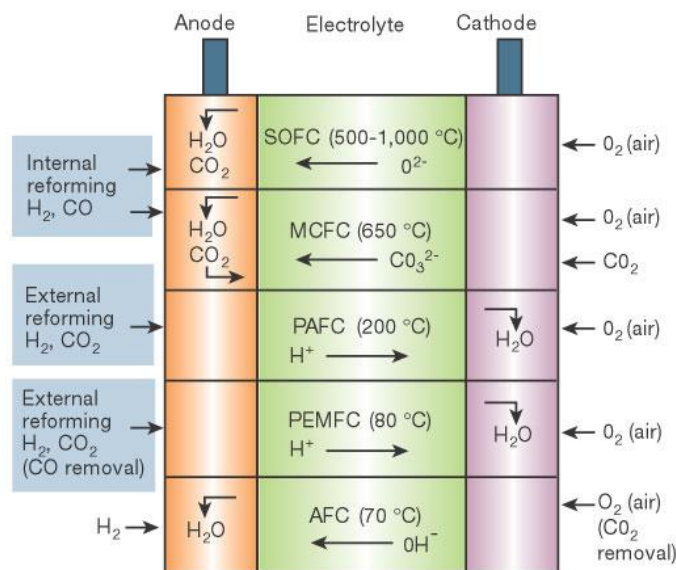
Figure 2.1: Some common types of fuel cells, their mobile ion and working temperature [31].

The most common fuel cell type today is the Polymer Exchange Membrane Fuel Cell (PEM-FC), which operates at low temperature (~80 °C). The main disadvantages with this technique is that it is limited to H_2 as a fuel, it is sensitive to contamination in the fuel (such as CO), and it requires expensive catalysts such as Pt [2, 3]. In contrast to the PEM-FC, the Solid Oxide Fuel Cell (SOFC), which operates at high temperatures (> 600 °C), can utilize a large variety of fuels (from H_2 to complex hydrocarbons such as diesel) without the need for expensive and limited catalysts [4, 6, 7].

2.1 Solid Oxide Fuel Cells (SOFCs)

The Solid Oxide Fuel Cell (SOFC) is based on an oxide-ion-conducting ceramic material as the electrolyte. Figure 2.1.1 illustrates the working principle of an SOFC during operation using H_2 as the fuel. Oxidation of the fuel (half reaction 1) takes place on the anode side and forms water vapour (and CO_2 if hydrocarbons are used as the fuel). At the same time, electrons are released and transferred through an external circuit to the cathode side where oxygen is reduced to oxygen ions (half reaction 2). The oxygen ions can then diffuse back through the oxygen-ion-conducting electrolyte to the anode side and react with the fuel. The overall reaction, when hydrogen is used as the fuel, is shown in reaction 3. The theoretical electric potential for a single cell; therefore, depends on the type of fuel utilized [1].

$$H_2 + O^{2-} \rightarrow H_2O + 2e^- \qquad (1)$$

$$\frac{1}{2}O_2 + 2e^- \rightarrow O^{2-} \qquad (2)$$

$$\frac{1}{2}O_2 + H_2 \rightarrow H_2O \qquad (3)$$
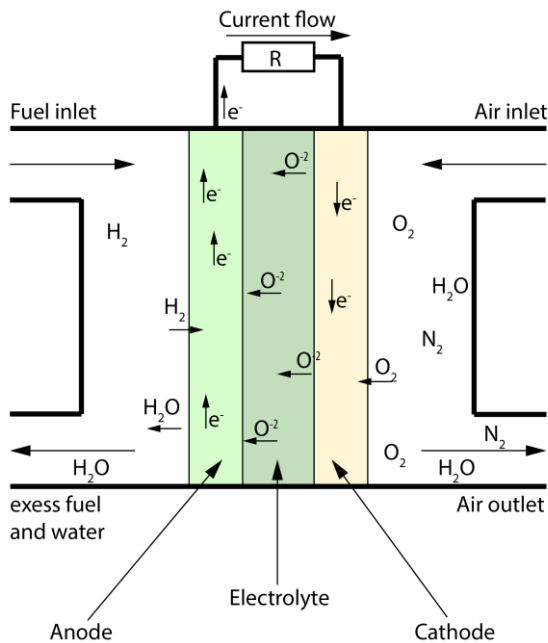
Figure 2.1.1: Operational concept of a Solid Oxide Fuel Cell (SOFC) [32]

The oxygen-ion-conducting electrolyte enables the use of several types of fuels such as H_2, NH_3, ethanol, natural gas, biogas and diesel. Furthermore, feedstocks, such as coal and biomass, can be gasified and utilized in an SOFC due to the high resistance towards impurities in the fuel [3, 6]. The possibility to utilize a broad variety of fuels has made the SOFC a possible candidate for a wide range of applications, ranging from a few kW in auxiliary power units to on-site power generation for residential and commercial applications and large scale MW power plants. Furthermore, very high electrical efficiencies ($> 60\,\%$) have been achieved for SOFC systems in the kW range [5]. Although the advantages of the SOFC are many, a few disadvantages have so far limited its commercialization. All of them are linked to the high operating temperatures which cause chemical and mechanical degradation during long-term operation and a mismatch in the thermal expansion coefficient between the system components which may cause damage

4

during heating and cooling. It is generally stated that a lifetime of at least 40 000 h (~5 years) with a degradation rate of less than 0.5 % per 1000 h must be guaranteed to make SOFC commercially attractive for stationary applications. Decreasing the operating temperature, improving the component materials and finding more economical manufacturing processes are some of the most important steps towards real commercialization of the SOFC.

2.2 Electrolyte and electrode materials

As mentioned in the previous section, the electrolyte material in an SOFC is a ceramic oxygen-ion-conducting material. The most common material today is Yttria or Scandia Stabilized Zirconia (YSZ respective ScSZ) [6]. Gadolina Doped Ceria (CGO) has also become a popular alternative enabling operation below 700 °C [3, 6, 7]. The electrolyte must be stable in both oxidizing and reducing atmospheres as well as gas tight [3, 6]. In contrast, the electrodes must be porous (and remain so during operation at high temperatures) to allow for gas flow and to increase the catalytic surface area. The anode must be a good electrical conductor and catalytically active, thus enabling oxidation of the fuel. A cermet consisting of nickel and the electrolyte material is considered to be the state of the art anode material today [3, 6]. As the anode material, the cathode material must be electrically conductive, but, at the same time, it needs to possess high oxygen-ion-conduction and be catalytically active towards oxygen reduction. Perovskite oxides, such as Strontium Doped Lanthanum Magnetite (LSM) and Lathanum Strontium Cobalt Ferrite (LSCF), are, therefore, frequently used as cathode materials [3, 6].

2.3 Interconnect

To increase the voltage of a fuel cell system, several cells are connected in series. Such an array of single cells is called a fuel cell stack (Figure 2.3.1). The interconnect, or what is frequently called the bipolar plate, is a current collector that separates the individual cells in a fuel cell stack. The main function of the interconnect is to electrically connect the anode to the cathode of the neighbouring cell and to separate the anode and cathode gases. This requires a gas-tight and electrically conductive material. The material must also be stable in both oxidizing as well as reducing atmospheres at high temperatures and have a Thermal Expansion Coefficient (TEC) similar to the other ceramic parts in the stack to avoid mechanical failure during start up and cooling down. Since cost is a major obstacle to the commercialization of SOFCs, this material must be economical to mass produce [8, 14].

Traditionally, ceramic materials such as $LaCrO_3$ have been used as the interconnect material. The development of new and thinner electrolyte and electrode materials has enabled a decrease in operating temperature below 800 °C, and the replacement of brittle and expensive ceramics with metallic interconnects. Replacing ceramics with metallic materials, such as stainless steels, significantly reduces large-scale production costs and increases both electrical and thermal conductivity. Today, ferritic stainless steels containing approximately 22 %wt. Cr, which has a thermal expansion coefficient close to the ceramic parts in the stack, have become the most popular choice as the interconnect material [8, 33].

Although metallic interconnects have several advantages over ceramic ones, some challenges attributed to high temperature corrosion need to be improved to guarantee stable long-term performance.
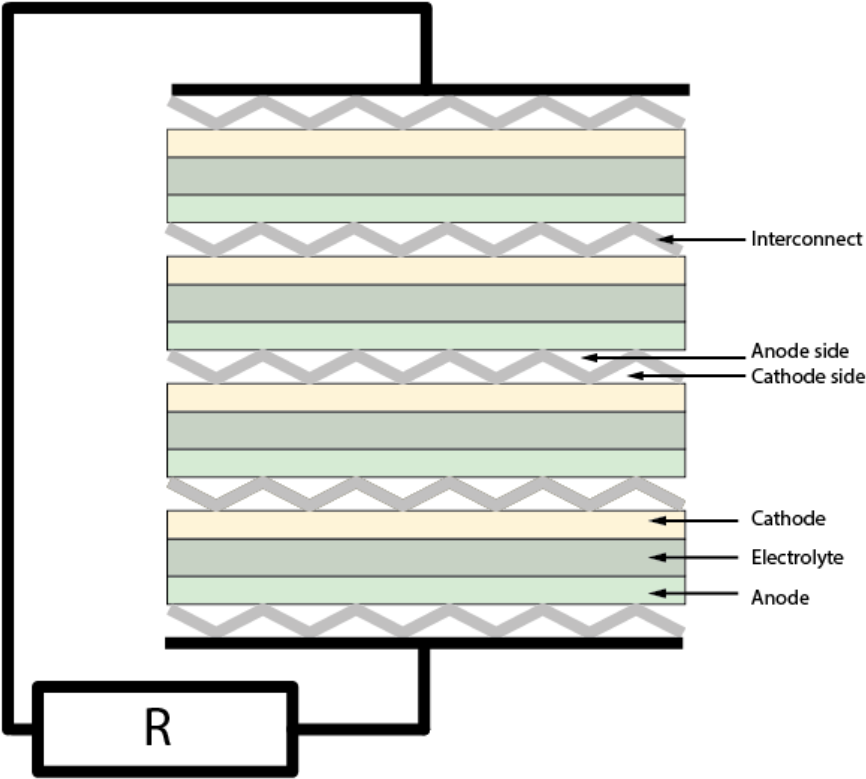
Figure 2.3.1: A planar SOFC stack consisting of four cells separated and electrically connected with interconnects [32].

3. Oxidation of metals

All metals, except a few noble metals, form metal oxides when they are exposed to an oxygen-containing atmosphere according to reaction 4 [34]:

$$xM(s) + \frac{y}{2}O_2(g) \leftrightarrow M_xO_y(s) \tag{4}$$

For this reason, the metal surface will immediately be covered by a metal oxide that separates the pure metal from the oxygen containing atmosphere. For further oxidation of the metal to occur, at least one of the reactants must penetrate the oxide scale [34]. Either the metal must be transported from the oxide-metal interface through the oxide scale to the oxide-gas interface or oxygen must be transported from the oxide-gas interface to the oxide-metal interface. Normally, both mechanisms take place simultaneously; however, one of them dominates. How fast a metal oxidizes is determined by the rate at which ions can penetrate the oxide scale.

3.1 Thermodynamics

Thermodynamics can predict if a metal will be oxidized or not at a certain temperature and in a certain environment as well as which type of metal oxide will be formed. At constant temperature and pressure, Gibbs free energy can be utilized to measure the stability of a system according to (5):

$$G = H - TS \tag{5}$$

Where G is the Gibbs free energy, H is the enthalpy, S the entropy and T the absolute temperature. The change in Gibbs free energy determines if the reaction is spontaneous ($\Delta G < 0$), in equilibrium ($\Delta G = 0$) or non-spontaneous ($\Delta G > 0$). Three phases are important to consider when a metal oxidizes, the metal, the metal oxide and the gas phase. The following equation can be utilized to reveal if a metal will oxidize or not (6):

$$\Delta G = \Delta G^0 + RT \ln K_{eq} = \Delta G^0 + RT \ln \frac{a_{(M_xO_y)}(s)}{a_{M(s)}^x a_{O_2(g)}^{\frac{y}{2}}} \tag{6}$$

Where ΔG^0 is the standard free energy change, R is the gas constant and K_{eq} is the equilibrium constant for the reaction, which can be described in terms of quota of the activities for the products and reactants. Since the activity for pure solids can be considered to be 1 and the activity of a gas can be expressed as its partial pressure (p_{O_2}), the change in Gibbs free energy at a certain temperature can be expressed as a function of oxygen partial pressure according to (7):

$$\Delta G = \Delta G^0 + RT \ln \frac{1}{p_{O_2}^{\frac{y}{2}}(g)} \tag{7}$$

This means that temperature and oxygen partial pressure determine if a metal will oxidize or not and which type of oxide is the most stable [35]. The stability of a metal oxide at a certain temperature and oxygen partial pressure can be illustrated using an Ellingham/Richardson diagram (Figure 3.1.1) [36]. It should be pointed out that there is an oxygen partial pressure gradient across the oxide scale giving rise to the possibility of a multi-layered structure, as is

the case when pure iron oxidizes [37, 38]. Thermodynamics; however, can only predict if a phase can exist in a certain environment and at a specific temperature under equilibrium conditions. How corrosion-resistant a metal or alloy is under these conditions depends on the rate of oxidation.
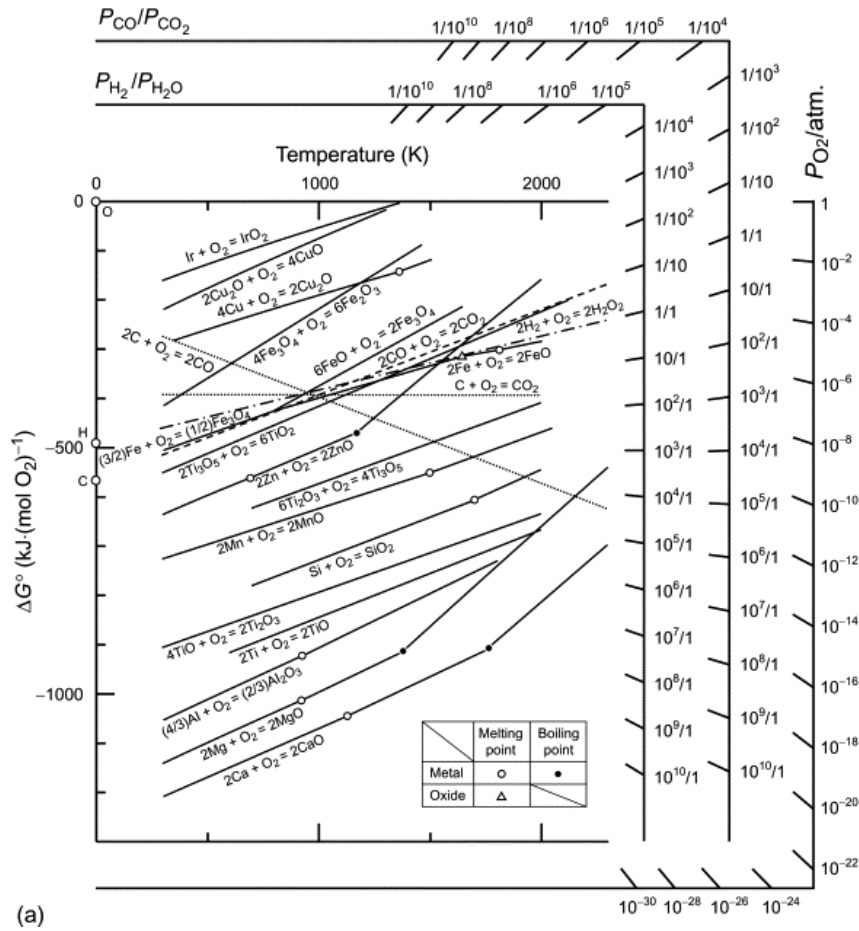
Figure 3.1.1: Ellingham/Richardson diagram for some metals and their metal oxides taken from [39].

3.2 Formation and growth of oxide scales

The formation and growth of an oxide scale can be separated into three steps (Figure 3.2.1) [34].
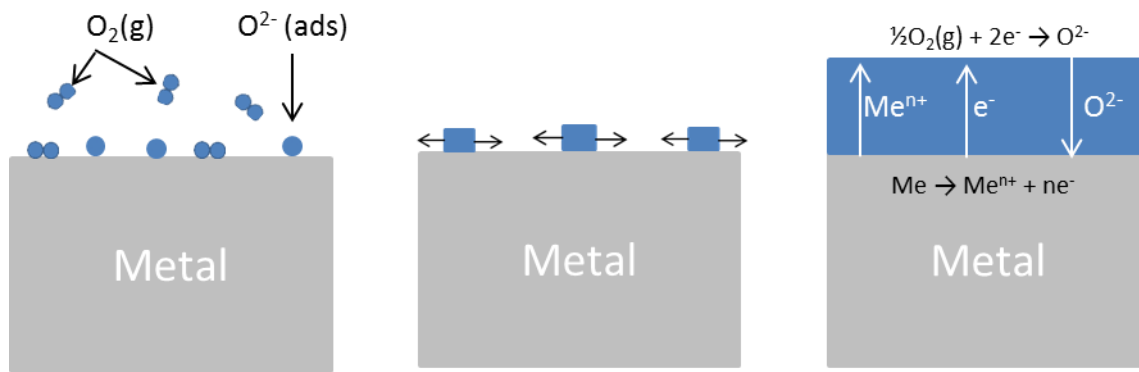
Figure 3.2.1: Schematic illustration of the formation (adsorption and oxide nucleation) and growth of an oxide scale.

In the first step, oxygen or water vapour molecules in the atmosphere adsorb on the metal surface by means of weak Van der Waals (VdW) interaction. The gas molecule, e.g. O_2, then dissociates into adsorbed O on the metal surface. This weak physical adsorption of O is followed by a charge transfer forming O^{2-} and Me^{n+} giving rise to an ionic bond between the oxygen and the metal. These chemisorbed oxygen ions then diffuse along the surface until a stable nucleus has been formed. Further adsorption followed by absorption leads to the growth of metal oxide nucleuses until a continuous layer of oxide covers the entire surface. From this stage on, further oxidation can only take place by means of solid state diffusion through the oxide scale [34]. For alloys containing several metals, all of the metals present at the surface will oxidize (if the oxide is thermodynamically stable). Due to the fact that different metals also show different growth rates, the one with the highest growth rate will overgrow the other(s) (assuming the concentration is high enough). However, if the metal in the slow-growing oxide (A) is less noble than the metal in the fast-growing oxide (B), it will reduce the fast growing metal oxide (BO) according to following reaction (8):

$$A \text{ (in alloy)} + BO \rightarrow AO + B \text{ (in alloy)} \tag{8}$$

This reaction will proceed until the less noble metal (A) has formed a continuous oxide layer (AO). From this moment on, the rate-limiting step for further oxidation is determined by solid state diffusion through the slow growing oxide (AO), consisting of the less noble metal (A) [35, 38]. However, if the activity of the less noble metal (A) is too low, no continuous oxide layer will form, and solid state diffusion through the fast growing oxide (BO) will be rate limiting [38].

What determines if an oxide scale is fast- or slow-growing depends primarily on the concentration of defects within the oxide scale [38]. All crystalline materials contain defects at all temperatures due to the minimization of free energy caused by the introduction of a certain amount of disorder [40]. The defect concentration in a certain material is; however, largely

dependent on enthalpy (it costs to break the bounds), and temperature. At higher temperatures, more disorder is introduced to the oxide, and more defects will be created where diffusion can take place. These rules are true for all materials; however, fast-growing oxides contain more defects than slow-growing oxides. It is important to keep in mind that there are several different types of defects within a dense oxide scale, such as point defects, dislocations and grain boundaries, and all of these influence the oxidation rate [34, 38, 41].

A defect can be a metal/oxygen vacancy or interstitial, or a substitutional impurity atom. Different oxides are classified according to the predominant type of point defect [34, 38]. The two most common slow-growing oxides, Al_2O_3 and Cr_2O_3, are classified as stoichiometric oxides. This is because the only stable oxidation state for both of them is III (e.g. Al^{3+} and Cr^{3+}). As a consequence, the only significant types of defects are Schottky and Frenkel defects [34]. In comparison, iron (Fe) can be both Fe^{2+} and Fe^{3+}. By reducing Fe^{3+} in Fe_2O_3 to Fe^{2+} oxygen vacancies must be introduced into the crystal lattice to maintain charge neutrality. Such oxides are often referred as anion-deficit oxides and tend to show much higher oxidation rates than stoichiometric oxides such as Cr_2O_3, Al_2O_3 and SiO_2. Another example of increased lattice defect concentration when a metal is stable in two oxidation states, is nickel oxide (NiO). Nickel normally forms Ni^{2+} in NiO, but can also be oxidized to Ni^{3+}. To maintain the charge balance, Ni^{2+} metal vacancies are created, and for this reason, this type of oxide is referred to as cation-deficit oxides. The formation of defects, such as cation or anion vacancies, in non stoichiometric oxides can explain why alloys forming an oxide scale that consists of Fe or Ni-oxide tend to oxidize faster than alloys forming a oxide scale that consists of a stoichiometric oxide such as Al_2O_3 or Cr_2O_3. Furthermore, as mentioned above, non-lattice defects, such as dislocations and grain boundaries, have a large impact on the rate of oxide scale growth. The diffusivity in polycrystalline materials can be ordered according to (9) [41]:

$$D \ll D_d \leq D_{gb} \leq D_s \tag{9}$$

Where D is the lattice diffusivity, D_d is the dislocation diffusivity, D_{gb} is the grain-boundary diffusivity and D_s is the diffusivity at the surface. This means that the quickest diffusion path through a dense oxide scale is via grain-boundary diffusion. For this reason, grain-boundary diffusion is commonly referred to as a short-circuit diffusion [34, 38]. Although grain-boundary diffusion is significantly faster than lattice diffusion, the volume in which grain-boundary diffusion can take place is very often small compared to the volume where lattice diffusion can take place. For this reason lattice diffusion will always be a part of the diffusion mechanism through the oxide scale. For the purpose of simplification, a general rule of thumb is that grain-boundary diffusion is the dominant diffusion path at temperatures below 0.6 of the melting temperature of the oxide [41]. At higher temperatures, lattice diffusion is considered to be the dominant diffusion path. In this thesis, Cr_2O_3-forming alloys were investigated at 650-850 °C. Cr_2O_3 has a melting point above 2400 °C which means that grain boundary diffusion should be considered to be the main diffusion path.

3.3   Oxidation kinetics
The growth of an oxide scale on a metal or alloy surface can be rather complex and is, in most cases, a mixture of several different mechanisms such as outward cation diffusion and inward

oxygen diffusion. Not only do ions diffuse within the lattice (as discussed above), but the flux of ions through a dense oxide scale is the sum of diffusion via the bulk, dislocations and grain boundaries. For this reason, the combined oxidation process is generally illustrated as a plot of oxide scale thickness against exposure time [34, 35, 38]. However, this has some practical limitations. Instead, a more common way to describe the oxidation process is to plot mass gain as a function of time, assuming that the gain in mass corresponds to the growth of an oxide scale [35]. Depending on the shape of such a mass gain plot, the growth of the oxide scale is normally said to show linear, logarithmic or parabolic oxidation behaviour (Figure 3.3.1) [34, 35, 38].
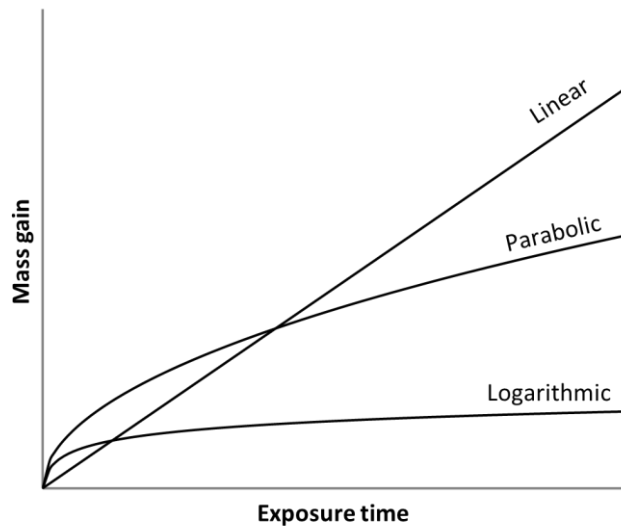
Figure 3.3.1: Mass gain curves illustrating linear, parabolic and logarithmic mass gain behaviour.

Linear rate law

If the mass gain as a function of time is linear (Figure 3.1.1), the gain in mass can be described according to (10):

$$\Delta m = k_l t \qquad (10)$$

Where Δm is the mass gain, k_l is the linear rate constant and t is the exposure time. This behaviour is commonly observed under conditions where a surface or phase-boundary process is the rate-determining step [38]. In such a case, diffusion through the oxide scale is not the rate-limiting step, and, therefore, is commonly observed if the oxide is porous or very thin. Linear mass gain behaviour can also be observed if the thickness of the protective oxide scale is constant.

Logarithmic rate law

If the mass gain as a function of time shows logarithmic behaviour (Figure 3.3.1), the mass gain is described according to the following equation (11):

$$\Delta m = k_{log} \log(t + t_0) + A \qquad (11)$$

Where Δm is the mass gain, k_{log} is the parabolic rate constant, t is the exposure time and A is the integration constant. This is generally only observed at very low temperatures and on extremely thin oxide scales [34, 38]. Electrons can, in this case, be transferred from the metal to the gas-oxide surface by quantum mechanical tunnelling though the oxide scale. After a certain time period, the oxide scale will become too thick for this mechanism to proceed. Due to the low temperatures, solid state diffusion will be too slow for continued growth, and the result will be that the rate drops to almost insignificant levels [38].

Parabolic rate law

The most common oxidation behaviour for high temperature alloys is parabolic behaviour (Figure 3.3.1) [34]. If an alloy shows parabolic behaviour, the mass gain is described according to the following equation (12):

$$\Delta m^2 = k_p t + A \tag{12}$$

Where Δm is the mass gain, k_p is the parabolic rate constant, t is the exposure time and A is the integration constant. Parabolic behaviour is observed when oxide-scale growth is controlled by solid-state diffusion through the scale [34, 35, 38]. The thicker the oxide scale becomes, the slower the diffusion though the scale, which leads to parabolic behaviour. Parabolic behaviour is generally observed if a metal or alloy forms a continuous, well-adherent and dense oxide scale.

3.4   Cr Vaporization

Some metals tend to form volatile species at high temperatures, enabling the breakdown of the protective oxide scale [35, 42]. Chromium is such a metal. It forms volatile Cr(VI) species in an oxidizing atmosphere. In dry oxygen, gaseous $CrO_3(g)$ will be formed according to reaction 13. At temperatures below 1000 °C, the vapour pressure of $CrO_3(g)$ is rather low and the vaporization of the oxide scale will normally not be a critical issue [12]. However, if water vapour is present, as in air, volatile chromium oxyhydroxides can form. Several authors have shown that the most abundant volatile chromium oxyhydroxide specie is $CrO_2(OH)_2$ [10-13], which is formed according to reaction 14.

$$Cr_2O_3(s) + 3O_2(g) \rightarrow 2CrO_3(g) \tag{13}$$

$$Cr_2O_3(s) + 2H_2O(g) + \frac{3}{2}O_2(g) \rightarrow 2CrO_2(OH)_2(g) \tag{14}$$
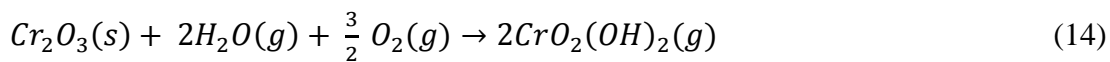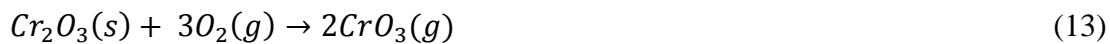
$CrO_2(OH)_2$ (g) has a much higher vapour pressure in air at temperatures below 1000 °C than $CrO_3(g)$. Hilpert et al. [12] have shown that even if water vapour content was as low as 2 % in air, $CrO_2(OH)_2(g)$ will still remain, by far, the most abundant Cr specie at temperatures below 1000 °C (Figure 3.4.1).
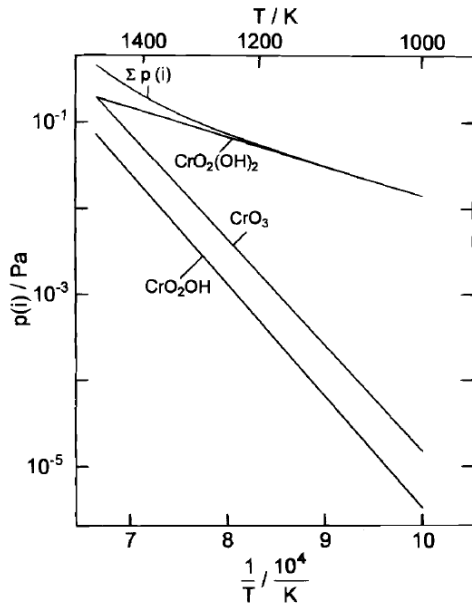
Figure 3.4.1: Partial pressures of the most abundant Cr-containing species over Cr_2O_3(s) in humid air $[p(O_2) = 2.13*10^4$ Pa, $p(H_2O) = 2*10^3$ Pa] at different temperatures taken from [12].

The rate of Cr vaporization is dependent on the rate of gas flow. Figure 3.4.2 illustrates the effect of gas flow rate on Cr vaporization at 850 °C in air + 3% H_2O from a 22% Cr steel. If the gas flow rate is low, Cr vaporization is in the equilibrium regime, meaning that volatilization is proportional to the rate of gas flow, and the result will be a linear region at low flow rates. Utilizing the slope of the curve at low flow rates the partial pressure of $CrO_2(OH)_2$ over the samples was calculated to $2*10^{-8}$ atm [28]. At higher flow rates, a plateau can be observed ($\sim$6000 sml min^{-1}). This region is referred to as the flow-rate-independent region. At this stage, the rate of Cr vaporization is instead limited by the kinetics of forming $CrO_2(OH)_2$(g).
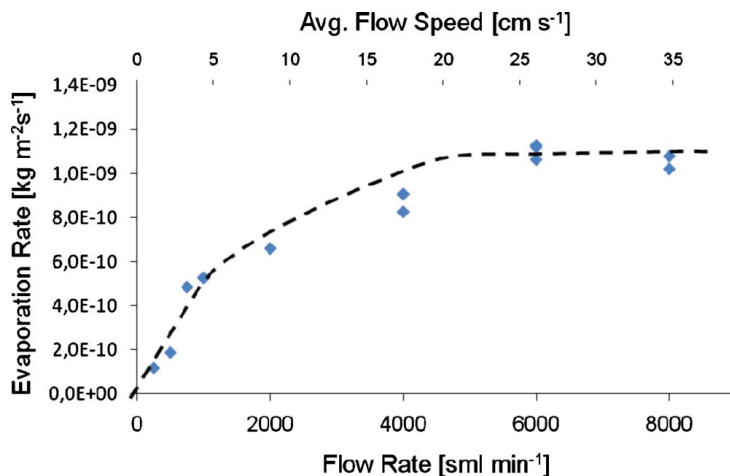
Figure 3.4.2: Rate of Cr vaporization as a function of gas flow rate at 850 °C in air + 3% H_2O on a 22% Cr steel [28].

3.4.1 Paralinear oxidation

Vaporization of the oxide scale can have a significant influence on oxidation behaviour. Tedmon [42] has described the phenomenon when a metal or an alloy shows parabolic oxide

13

scale growth, but is simultaneously subjected to vaporization of the oxide scale. The total sum of the oxide scale thickness or mass gain is then a combination of two processes: (i) Parabolic oxide-scale growth by solid state diffusion through the oxide scale, and (ii) loss of the oxide scale due to volatilization. Initially, when the oxide scale is thin, scale growth is faster than vaporization giving rise to parabolic oxidation behaviour. However, after a certain oxide scale thickness, the oxide-scale growth rate is reduced to the same rate as the vaporization of the oxide scale. At this stage, the so called limiting scale thickness has been reached and the oxide scale thickness remains constant. This gives rise to a mass gain behaviour called paralinear behaviour (see Figure 3.4.1.1). Initially, mass gain behaviour is parabolic, but after a certain period of exposure, parabolic mass gain behaviour turns into a linear mass loss, according to equation 15:

$$\Delta m = k_p \sqrt{t} - k_v t \qquad\qquad (15)$$

Where Δm is the mass gain, k_p is the parabolic rate constant, k_v the vaporization constant and t is the exposure time.
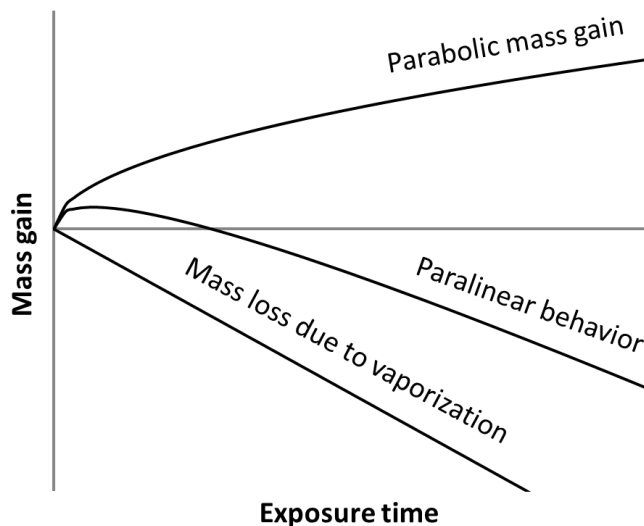
Figure 3.4.1.1: Paralinear mass gain behaviour illustrated as a combination of parabolic mass gain and linear mass loss due to vaporization.

3.5   Corrosion related to ferritic steels as interconnect material in SOFC

Good electrical conductivity is one of the main requirements for an interconnect material. Since an electric current will pass through the interconnect-electrode interface, the growth of an oxide scale is by far the largest contribution of the interconnect to electrical resistance if steels are used as the interconnect material. For this reason, steels that form a protective layer of electrically insulating Al_2O_3 or SiO_2 cannot be used as the interconnect material in an SOFC. Instead, Cr_2O_3-forming steels which conduct fairly well at elevated temperatures have become the most popular choice of interconnect material for planar SOFCs operating at 600-800 °C. Moreover, steels that form a protective Cr_2O_3 scale are generally considered to possess good high-temperature corrosion resistance in air. The problem remains that SOFC systems must guarantee a lifetime of at least five years without major degradation rates. During such long

operating periods, Cr_2O_3-forming steels tend to form oxide scales in the μm-range. Although electrical conductivity is fairly high at elevated temperatures; such thick oxide scales will significantly increase electrical resistance and decrease the performance of the SOFC. For this reason, improving the high temperature corrosion resistance of Cr_2O_3-forming steels is crucial to enable stable long-term performance and to prevent the breakaway corrosion which leads to the rapid degradation of an SOFC.

Oxide scale growth is not the only degradation mechanism associated with Cr_2O_3-forming steels as the interconnect material. Vaporization of Cr(VI) species, as described in Section 3.4, is also associated with rapid degradation in an SOFC. Cr at the interconnect surface can be transported to the electrolyte-cathode-gas interface called the Triple-Phase-Boundary (TPB), through vaporization as well as diffusion [17, 43-46]. The volatile Cr(VI) specie may then be reduced back to Cr(III) at the TPB, forming a deposit that blocks the electrochemical oxygen reduction process that takes place at the TPB [14-17]. For this reason, also mitigating the vaporization of Cr is crucial to enable stable long-term SOFC performance.

3.5.1 Steels specially developed as interconnect material in SOFC Systems

Chemical composition, steel microstructure and surface pre-treatment are some of the most important factors that determine if a steel will demonstrate protective behaviour (slow growing oxide) or not in a certain environment. Crofer 22 APU, Crofer 22 H, Sanergy HT and ZMG232 G10 are four of the most common commercially available ferritic stainless steels, specially developed as interconnect material for SOFC systems. These steels have four things in common: (i) To ensure the formation and growth of a protective Cr_2O_3 layer during long-term operation of an SOFC system, these steels contain approximately 22 %wt Cr. A higher amount of Cr may further improve long-term corrosion resistance; however, a brittle sigma phase may form during operation which is undesirable. (ii) Due to the requirement for low electrical resistance, the formation of a continuous layer of SiO_2 must be avoided. Si is, therefore, removed during the manufacture of the two steels Crofer 22 APU and ZMG232 G10. This process is expensive, therefore Nb and Mo or W is added to the two steels Sanergy HT and Crofer 22 H. These alloying elements form Laves-phase precipitates which bind the Si. The formation of Laves-phase precipitates also increases the high temperature creep strength of the steel. (iii) Small amounts of Mn (0.3 - 0.5 %wt) are added for the formation of a continuous $(Cr,Mn)_3O_4$ top layer which reduces the vaporization of Cr species. (iv) All four steels contain small amounts of Reactive Elements (RE). The addition of reactive elements, such as Ce, La, Y, Hf and Zr, are known to significantly improve the high temperature corrosion resistance of Al_2O_3 and Cr_2O_3-forming steels [47, 48]. Several mechanisms have been proposed in an attempt to explain the reactive element effect, but the most frequently discussed effect is a change in the oxide growth mechanism, which often occurs as a direct result of reduced outward cation diffusion [49-53]. It has also been shown that treating the surface of a ferritic Cr_2O_3-forming stainless steel with reactive elements, or applying a reactive element coating, can further improve high-temperature corrosion resistance [29, 30, 54, 55].

3.5.2 Reducing Cr vaporization

As mentioned in Section 3.5.1, ferritic stainless steels alloyed with small amounts of Mn have been specially developed as the interconnect material in SOFC systems to promote the

formation of a continuous $(Cr,Mn)_3O_4$ top layer. This has been shown to reduce Cr vaporization by a factor 2-3 compared to alloys that form a top layer consisting of almost entirely Cr_2O_3 [46, 56]. However, significant amounts of Cr are vaporized which poisons the cathode [16]. Therefore, the Cr vaporization rate must be decreased further to enable stable long-term performance. Today, the majority of all interconnect steels are coated with either a ceramic or a metallic coating. Metallic coatings are oxidized at elevated temperatures in air, and, thus, are turned into ceramic coatings (conversion coatings) [25]. Due to the requirement for low electrical resistance, the ceramic coating must be a good electrical conductor. Several electrically conductive spinel- and perovskite-type coatings have been suggested as promising coating candidates. Today, the most frequently used coating system is probably the $(Mn,Co)_3O_4$ (MCO) coating, which is a good electrical conductor at high temperatures. Several studies have also shown that a $(Mn,Co)_3O_4$ coating significantly decreases Cr vaporization [25, 27-30, 57]. Several techniques can be utilized to apply such a coating. Spray drying, dip-coating, screen printing, aerosol spray deposition, plasma spraying or Physical Vapour Deposition (PVD) can be used to apply $(Mn,Co)_3O_4$ coatings [18-24]. However, a steel can also be coated with metallic Co using PVD or electroplating [25-27, 58]. In such a case, Co will oxidize when the SOFC is heated in air and forms Co_3O_4. If the steel contains Mn, Co_3O_4 can turn into $(Mn,Co)_3O_4$ due to the outward diffusion of Mn from the steel.

4. Materials and methods

4.1 Materials

In the present thesis, three different ferritic stainless steels specially developed as interconnect material for SOFCs were investigated. Table 4.1 shows the chemical composition of the three steels studied.

TABLE 4.1.1: Composition of the studied steels in weight %. as specified by the manufacturer for the batches used.

Material	Manufacturer	Fe	Cr	C	Mn	Si	Mo	W	Nb	Add
Sanergy HT Batch: 531816	AB Sandvik Materials Technology	Bal.	22.4	0.01	0.25	0.07	0.93	<0.01	0.41	Zr
Crofer 22H Batch: 161061	ThyssenKrupp VDM	Bal.	22.9	0.007	0.4	0.2		1.9	0.5	La
Crofer 22 APU Batch: 4146	ThyssenKrupp VDM	Bal.	22.9	0.004	0.38	0.01				La

All samples were cut into 15 x 15 mm^2 coupons with a steel thickness of either 0.2 (Sanergy HT and Crofer 22 H) or 0.3 mm (Crofer 22 APU). All samples were exposed in an as-received state after being cleaned in acetone and ethanol using an ultrasonic bath. In Paper I only uncoated materials were studied. In Papers II and III; however, coated materials were investigated and compared to the uncoated material. The coatings were prepared at Sandvik Materials Technology using a Physical Vapour Deposition (PVD) process. Some of the materials investigated in Paper II were mechanically deformed. Mechanical deformation was conducted at Topsoe Fuel Cell where the steel foils were pressed into real interconnect shapes. Figure 4.1.1 shows the four types of samples studied in Paper II; (i) uncoated and undeformed, (ii) Co-coated and undeformed, (iii) deformed, and, subsequently, Co-coated as well as (iv) Co-coated, and, subsequently, deformed.
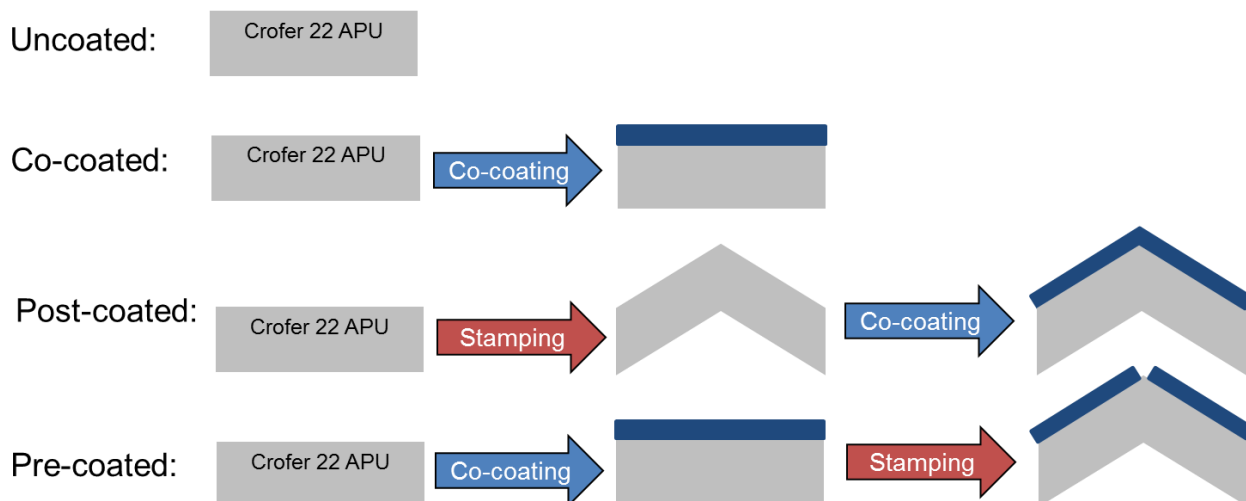
Figure 4.1.1: Schematic drawing of the four different materials investigated in Paper II.

4.2 Exposures

All exposures were carried out in a horizontal tubular quartz reactor with an inner diameter of 46 mm (Figure 4.2.1).
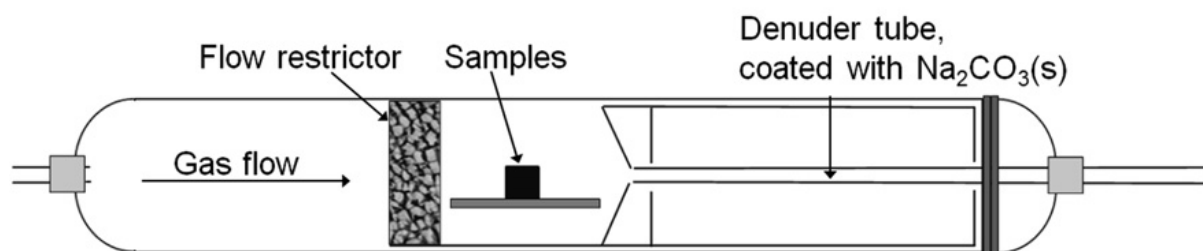
Figure 4.2.1: Schematic drawing of the experimental setup [28].

The exposure environment was the same in all three papers; air-3% H_2O atmosphere corresponding to the environment on the cathode side in an SOFC. 3% H_2O was achieved by bubbling dried and cleaned air through a warm-water bath connected to a condenser, which was set at 24.4 °C. The flow rate was set to 6000 sml min^{-1} to ensure a flow-independent regime in the reactor, as can be seen in Figure 3.4.2 [28]. In order to minimize natural convection, and to ensure a more uniform flow pattern, a porous silicon carbide flow restrictor was placed in front of the samples. Figure 4.2.1 shows that a denuder tube made out of quartz was placed behind the samples to act as the reactor outlet. The inside of the denuder tube (6 mm ID) was coated with Na_2CO_3(s). Volatile Cr(VI) species formed at the sample surface were transported with the gas stream through the coated denuder tube where sodium chromate was formed according to reaction 16.

$$CrO_2(OH)_2(g) + Na_2CO_3(s) \rightarrow Na_2CrO_4(s) + H_2O(g) + CO_2(g) \qquad (16)$$
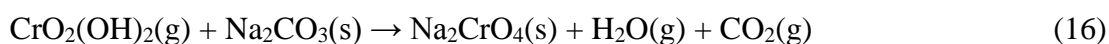
The advantage of this technique is that the denuder tube can be replaced regularly and rinsed with water, without affecting the samples. The amount of vaporized Cr was then quantified using spectrophotometry (Evolution 60S, Thermo Scientific). A more detailed description of the denuder technique can be found elsewhere [28].

5.   Analytical techniques

Gravimetric measurements were made using a six-decimal balance. The average net mass gain (change in mass before and after exposure) was calculated from the samples exposed simultaneously. The microstructure and chemical composition of the samples were analysed using Scanning Electron Microscopy (SEM) and Energy Dispersive X-Ray analysis (EDX). In Paper II, Focused Ion Beam (FIB) milling was additionally used on one selected sample to prepare a thin lamella for EDX analysis. X-Ray Diffraction (XRD) was used in Paper I to identify the crystalline phases present in the oxide scale, and spectrophotometry was used in all paper I and II for the quantification of Cr vaporization.

5.1   Scanning Electron Microscopy (SEM)

Today Scanning Electron Microscopy (SEM) is a very common tool used for microstructural surface characterization. In contrast to optical light microscopy, SEM is not limited by the wavelength of optical light, and can, therefore, reach much higher resolutions than optical microscopy. A focused beam of electrons, called the primary beam, is created in the electron gun. When the electrons of the primary beam penetrate the surface of a material, the sample material gives up energy which is emitted from the sample surface in different forms such as secondary electrons (SE), backscattered electrons (BSE) and characteristic X-rays (EDX). By scanning the sample surface, a virtual SEM image of the sample surface can be constructed.

Secondary Electrons (SE)

When the primary beam penetrates the sample surface, electrons are ejected from the sample surface (Figure 5.1.1). These electrons are called secondary electrons. Secondary electrons tend to have very low energy, and, therefore, can only escape from the outer-most part of the sample (Figure 5.1.2) which is why they offer the best imaging resolution.
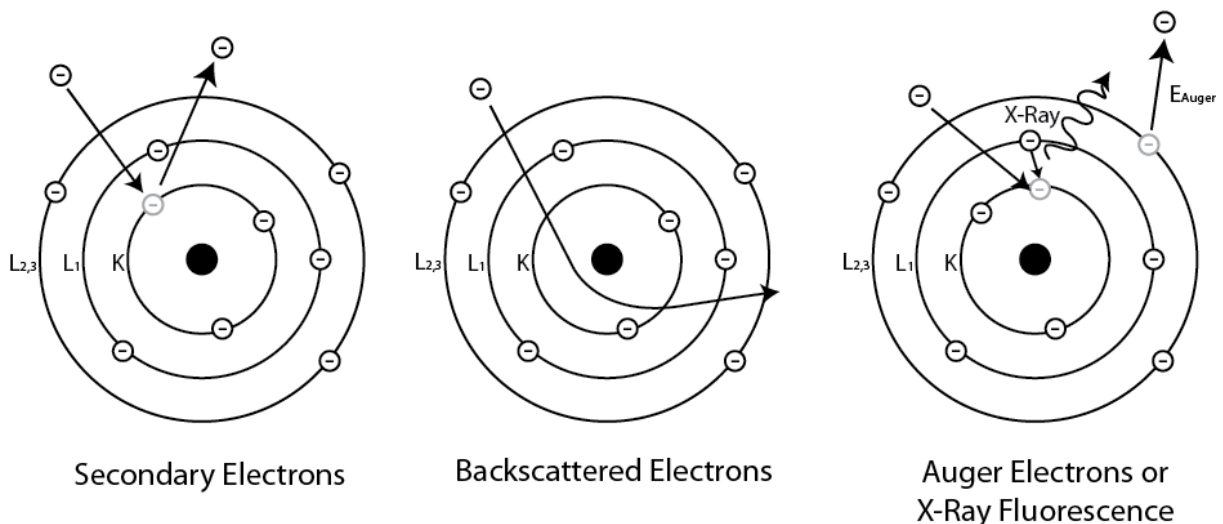
Figure 5.1.1: Schematic drawing of how secondary electrons, backscattered electrons and characteristic X-rays are formed in an SEM [59].
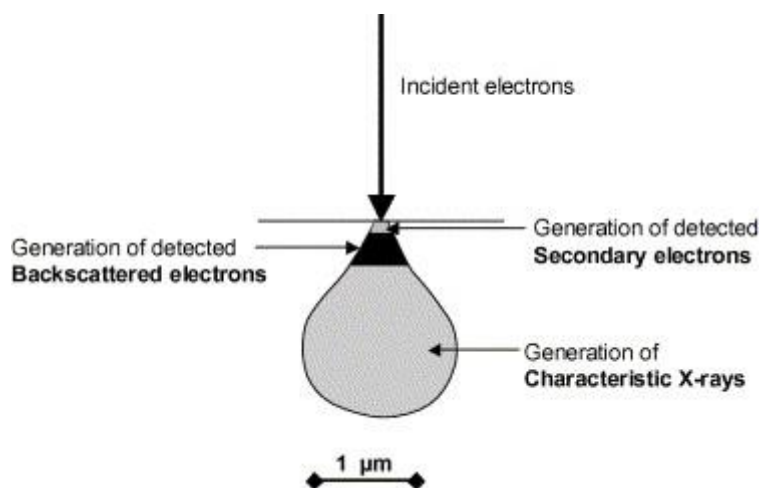
Figure 5.1.2: Interaction volume between the incoming electron beam and the specimen [60].

Backscattered Electrons (BSE)

In contrast to secondary electrons, backscattered electrons are electrons from the primary beam that have been scattered back off the sample surface by means of elastic collisions with the nuclei of the atoms in the sample (Figure 5.1.1). They possess much higher energy than secondary electrons which results in a much larger interaction volume (Figure 5.1.2). For this reason, the resolution in a BSE image is not as good as in an SE image. However, the contrast in a BSE image is correlated to the atomic number of the sample atoms. More electrons are backscattered in materials with heavy elements. Thus a BSE image can give information about variations in the chemical composition of the sample surface.

Energy Dispersive X-Ray analysis (EDX)

X-Rays are generated when an electron with high energy ejects an inner shell electron from a sample atom. As a result, another electron with higher energy in an outer electron shell, will fill the vacancy and release energy as an X-ray photon (Figure 5.1.1). Each element has defined energy differences between their electron shells. These X-rays emitted from the sample material can be measured with an X-ray spectrometer. A spectrum can, thus, be constructed by plotting the amount of X-rays as a function of the energy. As with secondary and backscattered electrons, a virtual image, showing the elemental composition of the surface, can be constructed by scanning the sample surface. However, it is important to keep in mind that X-rays can escape from a much larger distance in the sample material than secondary and backscattered electrons, as is illustrated in Figure 5.1.2.

5.2   Focused Ion Beam milling (FIB)

Ions can be used for the preparation of a cross section, or to cut out a thin lamella for SEM/EDX analysis or Transmission Electron Microscopy (TEM). This is done by focusing a high current ion beam, most commonly gallium (Ga) ions, at the surface. The high energy of the ions will sputter away the sample material, and by moving the beam, a cross section can be created in a selected area. FIB milling and lift-out technique was used in paper II to prepare a thin (electron transparent) specimen for EDX analysis. Due to the much thinner specimen, the interaction volume decreases significantly (Figure 5.1.2) and much better EDX resolution can be achieved.

5.3 X-Ray Diffraction (XRD)

X-Ray Diffraction (XRD) is a common analytical method utilized primarily to determine the phases present in a crystalline material. X-ray diffraction is based on the constructive interference of monochromatic X-rays and a crystalline material. When a material is hit with X-rays, these waves are scattered in all directions. Most of the scattered X-rays will not be in phase, and, as a consequence, will cancel each other out. However, some of them will be in phase (constructive interference). By stepwise changing the angle of the detector, increased intensity at angles specific for certain lattice parameters can be observed. Bragg´s law (Equation 17) is a mathematical relation between the angles at which constructive interference occurs and the distance between the atomic planes in a crystal.

$$2d \sin \theta = n\lambda \tag{17}$$

Where d is the spacing between the planes in the atomic lattice, θ is the angle between the incident ray and the scattering planes, n is an integer and λ is the wavelength of the incident wave.

By measuring the intensity of the scattered X-rays as a function of incident angle by utilizing monochromatic radiation, a diffraction pattern, specific for the lattice parameters of a material, can be observed.

XRD is mainly used for phase analyses of bulk materials. For this purpose, the Bragg-Brentano setup is the most common setup in which both the X-ray source and the detector move around the sample, allowing the angle of incidence and the angle of reflection to be the same. However, for XRD characterization of thin films, the X-ray source must be fixed at a low angle, otherwise the signal from the thin film will be too weak. For this reason, another setup, called the Grazing-Incidence setup is commonly used for thin film characterization. With this setup, the X-ray source is fixed at a specific angle (commonly < 5 ° depending on the thickness of the film), and only the detector moves around the sample.

5.4 Spectrophotometry

Spectrophotometry is an analytical technique which can be utilized to determine the concentration of light-absorbing ions or molecules in a solution. The basic principles of spectrophotometry is to allow monochromatic light pass through a cuvette containing a solution of light-absorbing ions or molecules, and measure the intensity of transmitted light with a photometer. The absorbance can then be calculated using the Beer-Lambert Law (18):

$$A = log_{10} \frac{I_0}{I} \tag{18}$$

Where A is the absorbance, I_0 is the intensity of the transmitted light for a given wavelength using the pure solvent, and I is the intensity of transmitted light through the solution. In this thesis, spectrophotometry was used to determine the concentration of CrO_4^{2-} ions in a water solution. Water solutions containing CrO_4^{2-} ions show a strong absorption peak around 370 nm, and, for this reason, monochromatic light at this wavelength was used for concentration measurements. By measuring the absorbance of several well-known CrO_4^{2-} ion standard solutions, an absorption factor could be calculated and used for the concentration analyses.

5.5 Area Specific Resistance (ASR) measurements

Area specific resistance (ASR) measurement is a technique used to measure the electrical resistance associated with a thermally growing oxide scale. Today, there are no standards for how to measure scale resistance; instead, every research group has their own way of measuring ASR. The most commonly used electrode material for ASR measurements is Platinum (Pt), although the use of LSM (in cathode environment) is becoming more popular, since this material is frequently used as the cathode material in an SOFC. In Paper III, ASR measurements were conducted. All ASR measurements were carried out at SMN/FERMiO, University of Oslo in Oslo, Norway. Pt was used as the electrode material and ASR was measured ex-situ (on pre-exposed samples). A DC Agilent 34401A nanovoltmeter was utilized for all measurements. Since there were two oxide scales on each sample coupon (one on each side), the ASR was calculated according to (19):

$$ASR = R_{measured} * A/2 \tag{19}$$

Where $R_{measured}$ is the measured electrical resistance and A is the contact area.

6. Results and discussion

6.1 The influence of temperature on Cr vaporization and oxide scale growth

Increased temperature is commonly used to accelerate high temperature corrosion mechanisms that are thermally activated such as oxide scale growth and Cr vaporization. Cr vaporization and oxide scale growth are; however, two separate mechanisms, and may, therefore, be influenced differently by an increase in temperature. The purpose of this study was, therefore, to separately investigate the influence of temperature on both mechanisms. Two commercially available ferritic stainless steels, Sanergy HT and Crofer 22 H, were selected and isothermally exposed for 24, 168 and 500 h at three temperatures (650, 750 and 850 °C). At 850 ºC both steels show parabolic mass gain behaviour (see Figure 6.1.1).
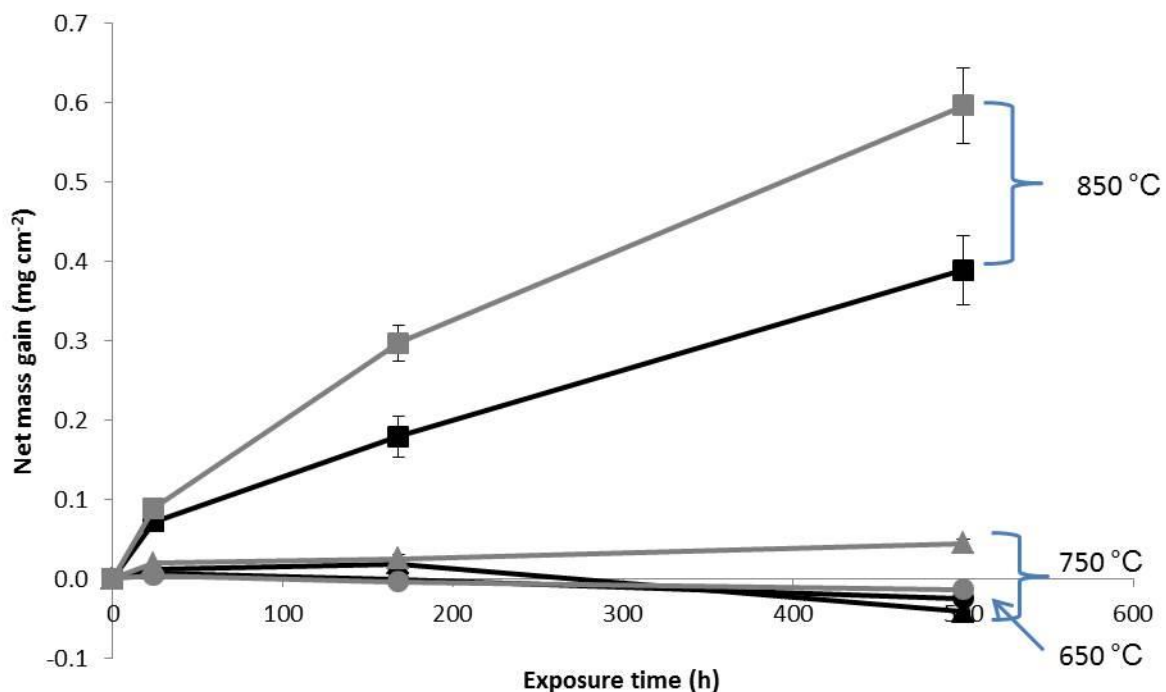
Figure 6.1.1: Net weight change for Sanergy HT (black) and Crofer 22 H (grey) isothermally exposed for 24, 168 and 500 h at 650 (dots), 750 (triangles) and 850 °C (squares) in air containing 3% H_2O (6000 sml min^{-1}).

Both steels had gained almost the same amount of mass after 24 h; however, with longer exposure time Crofer 22 H gained more mass than Sanergy HT. It is interesting to note that at lower temperatures (650 and 750 °C for Sanergy HT and 650 ºC for Crofer 22 H), negative mass gains were observed for both materials after 500 h. An increase in mass is generally correlated with oxygen reacting with the steel, and forming an oxide, i.e. scale growth. However, changes in net mass gain values may be misleading owing to factors such as vaporization or spallation of the oxide scale. None of the materials investigated showed any signs of spallation, and for this reason, the negative mass gain values seen at the lower exposure temperatures most probably is an effect of vaporization of the oxide scale. It should also be pointed out that both materials initially showed positive mass gain values at both 650 and 750

ºC. This behaviour, called paralinear behaviour, is commonly observed when a steel shows parabolic oxide scale growth, but is simultaneously subjected to vaporization of the oxide scale [42]. Cr vaporization measurements at the three exposure temperatures showed that a significant amount of Cr is vaporized during exposure at all three temperatures (Figure 6.1.2).
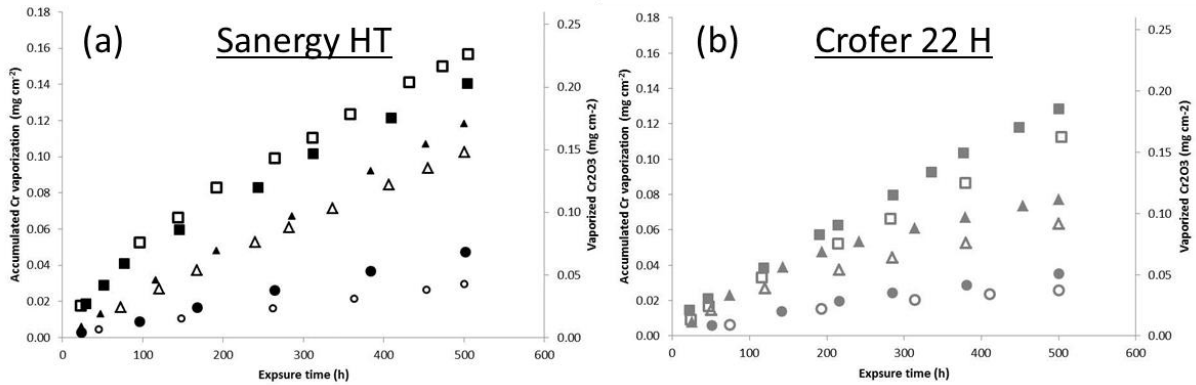
Figure 6.1.2: Accumulated Cr vaporization as a function of time for (a) Sanergy HT and (b) Crofer 22 H at 650 (dots), 750 (triangles) and 850 °C (squares) in air containing 3% H_2O (6000 sml min^{-1}). Filled and empty symbols represent the two individual isothermal exposures.

Both steels exhibited similar vaporization behaviour however, the amount of vaporized Cr was on average, 20-30 % lower after 500 h of exposure for Crofer 22 H irrespective of exposure temperature. Moreover, by comparing the amount of evaporated Cr with the net mass gain, it can be seen that Cr vaporization is less influenced by temperature than oxide scale growth. The change in mass gain behaviour from parabolic at 850 ºC to paralinear at 750 and 650 ºC is, therefore, assumed to be related to the weaker temperature dependency of Cr vaporization than oxide scale growth.

It can be concluded that a significant amount of the oxide scale had been vaporized during exposure at all three temperatures. By adding the amount of vaporized Cr (as Cr_2O_3) to the net mass gain values the gross mass gain (compensated for Cr vaporization) can be calculated (Figure 6.1.3). It can be concluded that when mass gain is compensated for Cr vaporization, both steels show positive mass gain values at all three temperatures, as would be expected. Furthermore, both steels behave parabolically at all three temperatures which indicates that solid state ion diffusion is the rate-determining mechanism for oxide scale growth. It is also interesting to note that both steels show more or less the same gross mass gain behaviour at 650 and 750 ºC which indicates that the lower mass gain values for the steel Sanergy HT at 750 ºC are entirely an effect of the higher amount of vaporized Cr at this temperature. The lower mass gain values for Sanergy HT at 850 ºC; however, cannot entirely be explained by a higher amount of volatilized Cr. Instead, the main reason for the lower mass gain for Sanergy HT at 850 ºC is the thinner oxide scale (Figure 6.1.5).
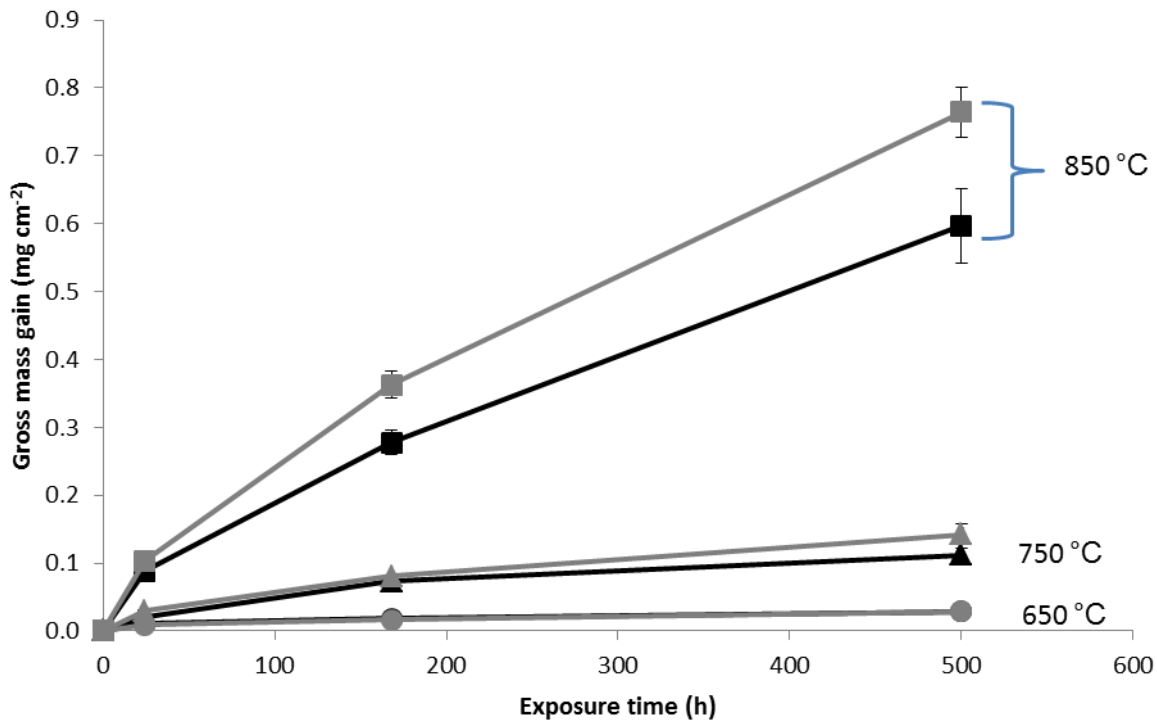
Figure 6.1.3: Gross (corrected for Cr vaporization) weight change for Sanergy HT (black) and Crofer 22 H (grey) isothermally exposed for 24, 168 and 500 h at 650 (dots), 750 (triangles) and 850 °C (squares) in air containing 3% H_2O (6000 sml min^{-1}).
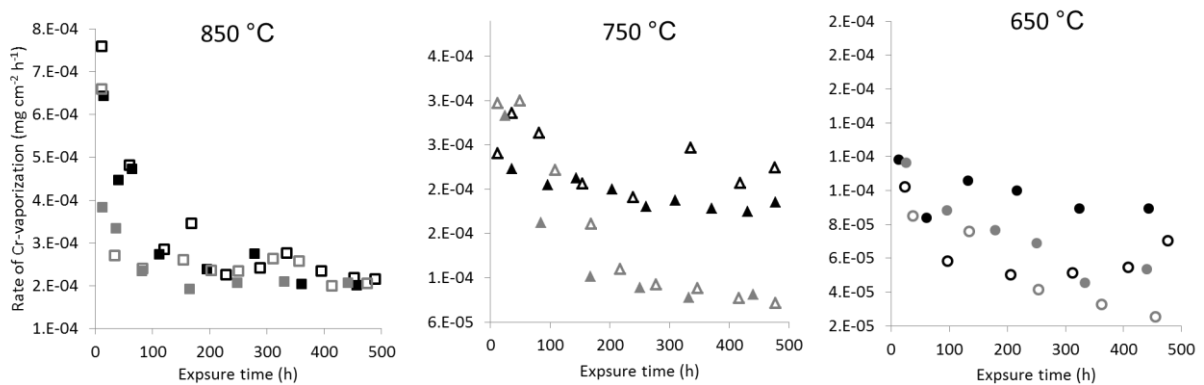
Figure 6.1.4: Rate of Cr vaporization as a function of time for Sanergy HT (Black) and Crofer 22 H (Grey) at 850, 750 and 650 °C in air containing 3% H_2O (6000 sml min^{-1}). Filled and open symbols represent the two individual isothermal exposures.

The rate of Cr vaporization is somewhat greater initially than after 500 h of exposure for both steels at all three temperatures (Figure 6.1.5). However, the amount of reduction as well as the time necessary to reduce the rate of Cr vaporization differed with exposure temperature and steel investigated.

A reduction in the rate of Cr vaporization is expected, since both materials contain small amounts of Mn and are, therefore, expected to form a top layer consisting of $(Cr,Mn)_3O_4$, which would reduce Cr activity at the surface. For this layer to be formed, Mn ions must diffuse out from the steel to the surface oxide layer by means of solid state diffusion through the inner Cr_2O_3 layer. A higher concentration of Mn in the steel may, therefore, accelerate the formation

of a continuous $(Cr,Mn)_3O_4$ top layer. This would agree with the more rapid decrease in Cr vaporization rate at 850 °C for the Mn-richer steel Crofer 22 H. It should; however, be mentioned that Mn concentration is not the only factor that can influence the flux of Mn ions. Other alloying elements, steel microstructure and surface treatment, are important factors that may influence the outward flux of Mn ions. Interesting to note is; however, that after a certain period of exposure both steels showed the same vaporization rate. After 500 h of exposure at 850 °C had both steels formed a continuous oxide scale consisting of an inner Cr_2O_3 layer and an outer $(Cr,Mn)_3O_4$ top layer (Figure 6.1.5).
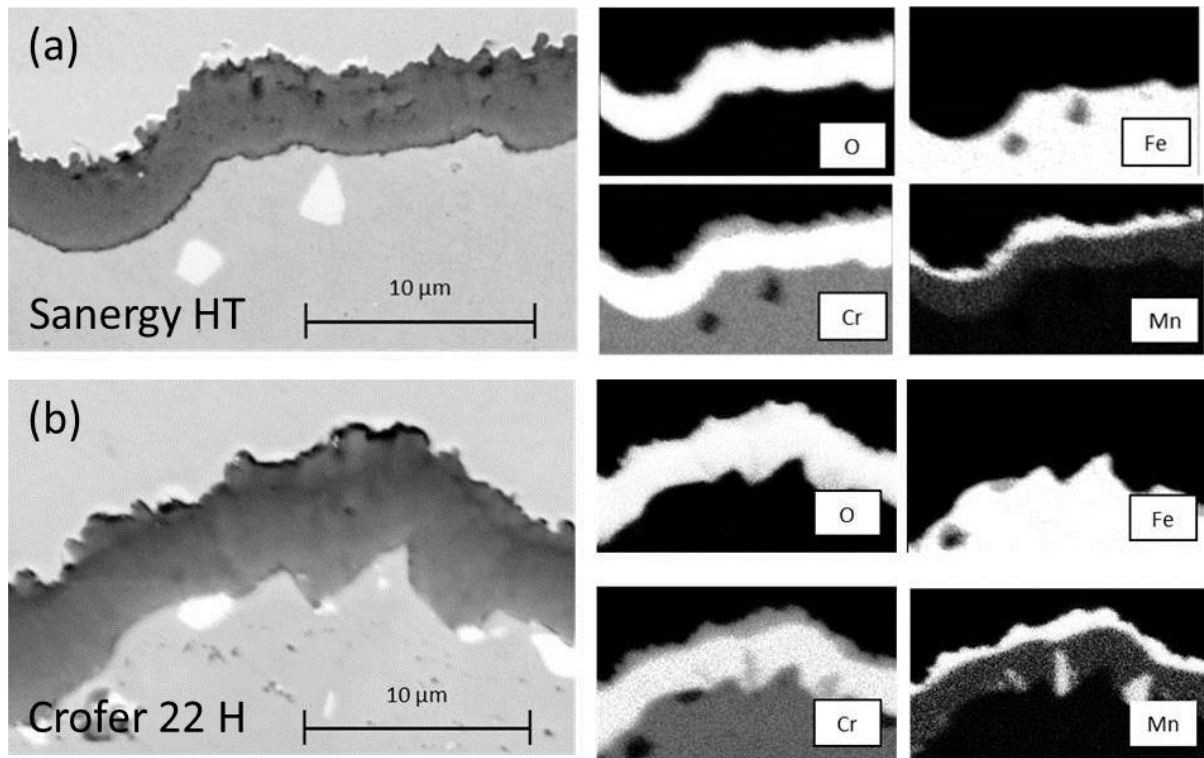
Figure 6.1.5: SEM cross section and EDX elemental maps of (a) Sanergy HT and (b) Crofer 22 H exposed for 500 h at 850 °C in air 3% H_2O (6000 sml min^{-1}).

Moreover, the thickness of the $(Cr,Mn)_3O_4$ top layer was rather similar for the two steels, which would explain why both steels tended to vaporize at the same rate after a certain period of exposure. These images also show that the inner Cr_2O_3 layer was somewhat thicker for Crofer 22 H after 500 h of exposure at 850 °C which would explain the higher mass gain for this material at 850 °C. Areas rich in both Cr and Mn, most probably $(Cr,Mn)_3O_4$, could additionally be observed at the steel-oxide interface for Crofer 22 H. Huczkowski et al. have also observed such areas and have proposed that these Mn-rich oxides are formed as a result of "crack-healing" [61].

When the temperature was decreased to 750 °C, a notable difference was observed between the two steels (Figure 6.1.4). Crofer 22 H clearly showed a tendency to reduce the rate of Cr vaporization whereas Sanergy HT only showed a small reduction initially. The much slower decrease in Cr vaporization rate for Crofer 22 H at 750 °C than at 850 °C is assumed to be correlated to a slower outward diffusion of Mn ions at the lower temperature. However, after

200-300 h, the rate levelled off to a value of $9*10^{-5}$ mg cm^{-2} h^{-1}, which is much lower than the approximately $2*10^{-4}$ mg cm^{-2} h^{-1} for Sanergy HT at 750 °C. These oxide scales were too thin for accurate EDX analysis however according to the XRD analysis both steels formed Cr_2O_3 and spinel-type oxide at 750 °C (see paper I).

From the data available, it is proposed that the much lower rate of Cr vaporization for Crofer 22 H than for Sanergy HT at 750 °C is due to differences in the $(Cr,Mn)_3O_4$ top layer thickness. It is assumed that vaporization of Cr takes place at the gas-oxide interface, and should, therefore, not be thickness-dependent if the chemical composition of the oxide scale is homogenous. However, since a growing oxide scale under the present conditions is not expected to be under equilibrium, a concentration gradient may be present within the oxide scale.

Due to rapid Mn outward diffusion from the steel and the loss of Cr as an effect of Cr vaporization (reaction 20), a chemical gradient may be present within the $(Cr,Mn)_3O_4$ top layer.

$$(1+x)Cr_2MnO_{4(s)} + 3xH_2O_{(g)} \frac{5x}{2}O_{2(g)} \rightarrow Cr_{2-x}Mn_{1+x}O_{4(s)} + 3xCrO_2(OH)_{2(g)} \tag{20}$$
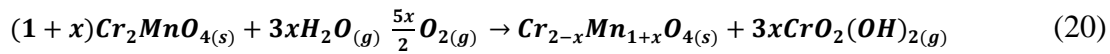
According to [62], is there great miscibility in $(Cr,Mn)_3O_4$ at elevated temperatures at which the Cr:Mn ratio can vary from 2:1 (Cr_2MnO_4) to 1:2 (Mn_2CrO_4). Canovic et al. [30] observed a chemical gradient for Sanergy HT in the $(Cr,Mn)_3O_4$ layer after 168 h in the same exposure environment as the present study. Froitzheim et al. [25] observed a thin outer Mn and Cr rich oxide, probably $(Cr,Mn)_3O_4$ as soon as after 1 h for Sanergy HT in the same exposure conditions. The rate of Cr vaporization at 850 °C clearly decreased during this 168 h for Sanergy HT at 850 °C. It is, therefore, proposed that this reduction in the Cr vaporization rate is associated with the growth of a $(Cr,Mn)_3O_4$ top layer. A thickening of the $(Cr,Mn)_3O_4$ top layer may induce a chemical gradient in the $(Cr,Mn)_3O_4$ layer, consequently decreasing the Cr concentration on the outermost surface layer.

Low voltage SEM images of FIB cross sections from Crofer 22 H and Sanergy HT after 500 h at 750 °C shows that the top layer, assumingly a spinel layer, is thicker for the Crofer 22 H than for the Sanergy HT at 750 °C (Figure 6.1.6). It is, therefore, suggested that the lower rate of Cr vaporization exhibited by the Crofer 22 H is associated with a lower Cr concentration in the outermost surface oxide as an effect of the thicker spinel top layer, as discussed above for the samples exposed at 850 °C.
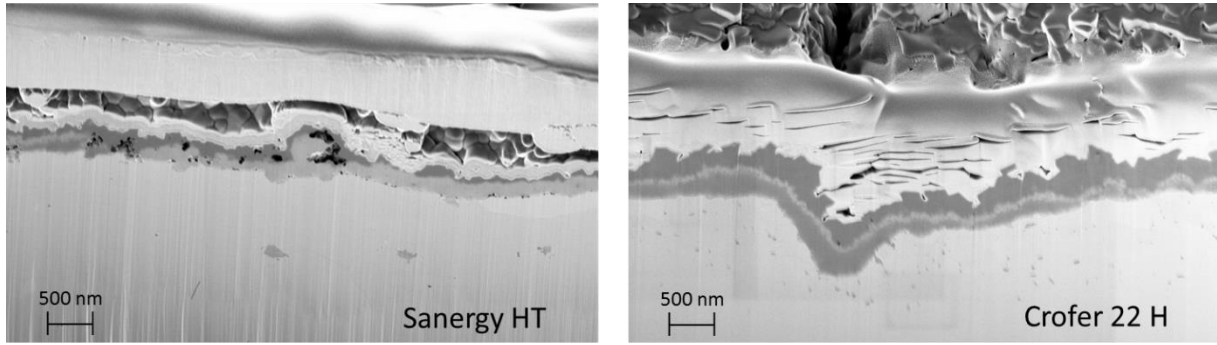
Figure 6.1.6: Low voltage SEM images of FIB cross sections from Sanergy HT (left) and Crofer 22 H (right) exposed for 500 h at 750 °C in air 3% H_2O (6000 sml min^{-1}).

When the exposure temperature was decreased even further to 650 °C, both steels showed similar vaporization rates (Figure 6.1.4). As at 750 °C, the oxide scales were too thin for accurate SEM/EDX analysis; however, both Cr_2O_3 and spinel-type oxide were detected on both steels oxidized at 650 °C for 500 h using the XRD technique (see paper I).

To be able to compare the effect of temperature on the two degradation mechanisms, oxide scale growth and Cr vaporization, the activation energy for both reactions was calculated using Equation 21.

$$\ln(k) = \frac{-E_a}{RT} + \ln(A) \tag{21}$$

Where k is the rate constant of a chemical reaction (oxide scale growth respectively Cr vaporization), E_a is the activation energy, R is the universal gas constant, T is the absolute temperature and A is the pre-exponential factor.

To calculate the activation energy for oxide scale growth, parabolic rate constants were calculated from the gross mass gain data (Figure 6.1.3). The relationship between mass gain and oxidation kinetics can be described using the Parabolic Rate Law (22).

$$\left(\frac{\Delta m}{A}\right)^2 = k_p t + C \tag{22}$$

Where, Δm is the mass gain, A is the sample surface area, t is the exposure time, C is the integration constant and k_p is the parabolic rate constant. Both steels showed parabolic behaviour which indicates that scale growth is controlled by solid state diffusion. The calculated rate constants values at 650, 750 and 850 °C (see paper I) are within the typical order of Cr_2O_3-forming materials [63-65]. From these values, activation energies of 261 and 283 kJ mol^{-1} for Sanergy HT and Crofer 22 H, respectively, were obtained.

These values agree well with other published activation energy values for the high temperature oxidation of Fe-Cr alloys in air [63, 66-68]. Activation energy values obtained from such parabolic rate constants are probably a combination of several mechanisms and specific for the alloys and exposure conditions. Some authors [63]; however, have compared similar values to

the 255 kJ mol^{-1} reported by Hagel and Seybolt [69] for cation diffusion in Cr_2O_3, and suggest that the oxide scale predominantly grows by means of the outward diffusion of Cr ions.

To calculate the activation energy for Cr vaporization, another type of exposure was carried out (Figure 6.1.7) which is described in paper I, since the isothermal exposures did not show Arrhenius-type behaviour. The non-Arrhenius-type behaviour is assumed to be due to differences in chemical composition and/or morphology at various temperatures.
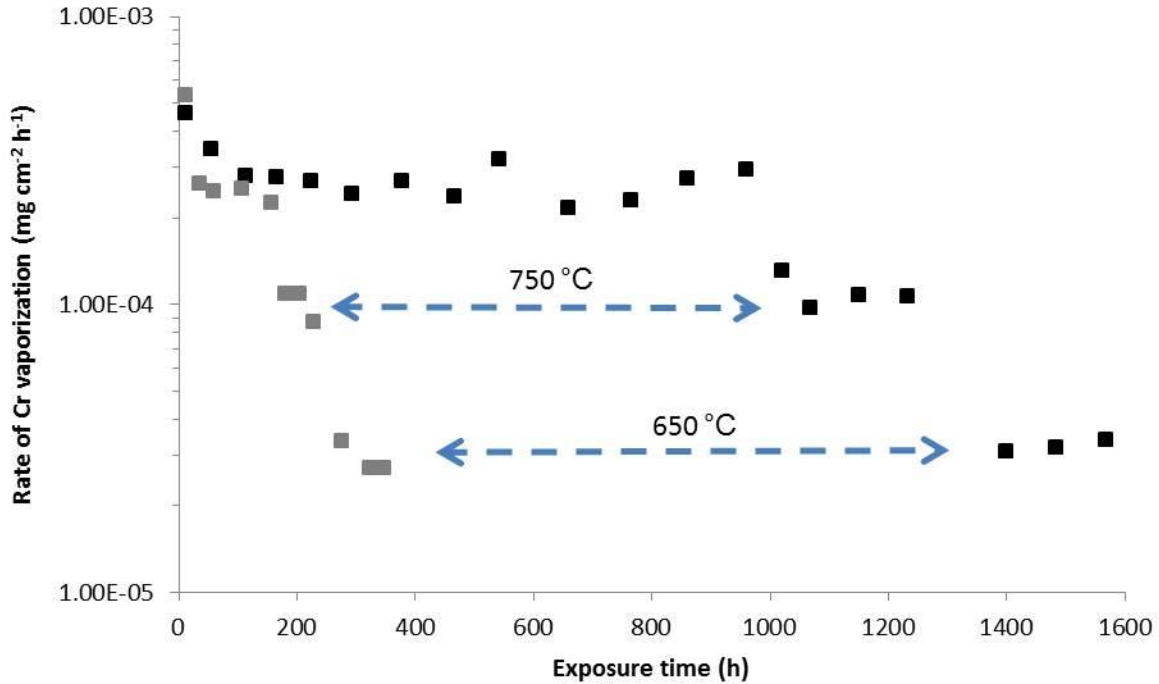
Figure 6.1.7: Rate of Cr vaporization for Sanergy HT (Black) and Crofer 22 H (Grey) at different temperatures in air containing 3% H_2O (6000 sml min^{-1}). The samples were initially exposed at 850 °C until the rate of Cr vaporization was constant. During the same exposure time period, Cr vaporization was also measured at 750 and 650 °C.

Using the rate of Cr vaporization obtained in these experiments, activation energies of 91 and 92 kJ mol^{-1} for Sanergy HT and Crofer 22 H, respectively, were obtained. These values are in good agreement with the 83 kJ mol^{-1} for Cr vaporization on a Cr_2O_3 surface theoretically calculated by Panas et al [70]. Since the activation energy for scale growth was approximately 3 times higher than the activation energy for Cr vaporization, it can be concluded that Cr vaporization is less influenced by temperature than by oxide scale growth.

The results presented in this study show that by reducing the temperature 100 °C, the amount of vaporized Cr only decreases by a factor 2-3, whereas the gross mass gain decreases by a factor of five. This results in a change in oxidation kinetics from parabolic to paralinear oxidation kinetics when the temperature is reduced from 850 to 750 and 650 °C. To ensure stable, long-term performance in an SOFC stack, high quality coatings that inhibit Cr vaporization are necessary, even if the operating temperature is decreased to temperatures as low as 650 °C.

6.2 Activation energy measurements for Cr vaporization on Cr_2O_3 and Co-coated Sanergy HT

Cr vaporization can be decreased significantly by coating a ferritic stainless steel with a thin layer of metallic Co [25-30]. Upon oxidation at elevated temperatures, the Co will rapidly oxidize to Co_3O_4, and if the steel contains Mn, a top layer of $(Co,Mn)_3O_4$ will be formed due to the outward diffusion of Mn from the steel [25]. A significantly lower Cr activity at the surface [25] and/or a significant lower equilibrium constant when Cr is vaporized from $(Co,Cr)_3O_4$ than from Cr_2O_3 [71] has been proposed as an explanation for the effectiveness of Co-coatings in supressing Cr vaporization. The purpose of this study was to determine the activation energy for Cr vaporization from a Co-coated steel and compare this value to the activation energy value obtained from the uncoated material in the previous section (6.1). As a reference, the activation energy for pure Cr_2O_3 was determined and compared to the theoretically calculated activation energy value for Cr_2O_3 reported by Panas et al. [70]. Cr vaporization was measured, in a non-isothermal manner (see paper I). The uncoated material (Sanergy HT), shown in the previous section, had formed a $(Cr,Mn)_3O_4$ spinel top layer before the temperature was reduced to 750 and 650 °C, and the 640 nm Co-coated Sanergy HT material, exposed for one week before the temperature was reduced, had formed a $(Co,Mn)_3O_4$ top layer according to [25, 30] (Figure 6.2.1).
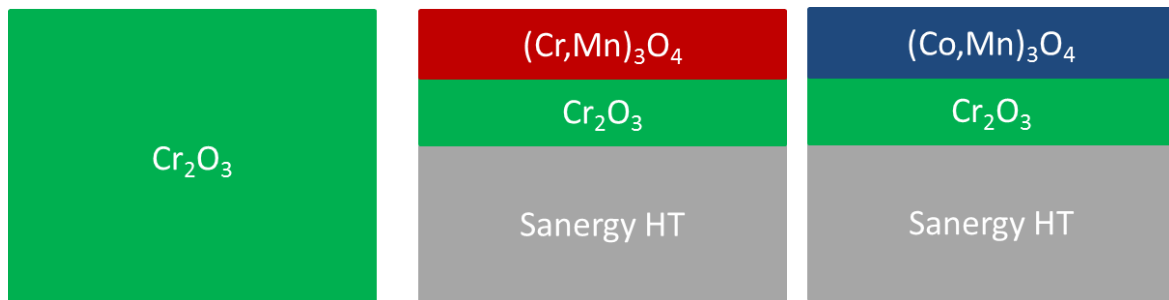
Figure 6.2.1: Illustration of the materials used for activation energy measurements. The uncoated and Co-coated materials were initially exposed at 850 ° C until a continuous top layer of $(Cr,Mn)_3O_4$ respectively $(Co,Mn)_3O_4$ was formed before the temperature was lowered to 750 and 650 ℃.

As expected, pure Cr_2O_3 evaporated more Cr than the uncoated steel, and the Co-coated evaporated even less at all temperatures (Figure 6.2.2). The calculated activation energies were 81, 91 and 70 kJ mol^{-1} for pure Cr_2O_3, uncoated Sanergy HT, and 640 nm Co-coated Sanergy HT, respectively.
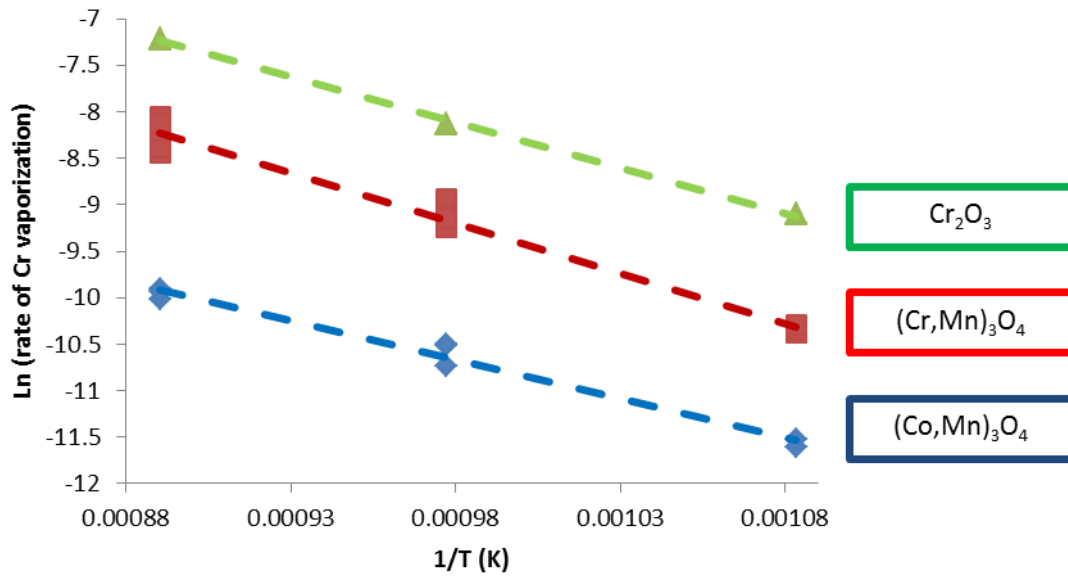
Figure 6.2.2: Arrhenius plot showing the influence of temperature on Cr vaporization in air containing 3% H_2O (6000 sml min^{-1}) for pure Cr_2O_3 (green triangles), uncoated Sanergy HT (red squares), and 640 nm Co-coated Sanergy HT (Blue diamonds).

The value of 81 kJ mol^{-1} obtained for the pure Cr_2O_3 material is very close to the theoretically calculated value of 83 kJ mol^{-1} obtained for Cr_2O_3 reported by Panas et al. [70]. Compared to the large difference in the activation energy between the two mechanisms, the Cr vaporization and oxide scale growth shown in the previous section (activation energy was approximately 270 kJ mol^{-1} for oxide scale growth and 90 kJ mol^{-1} for Cr vaporization), this is a rather insignificant difference between the three materials. Based on these measurements, it is, therefore, assumed that the Cr vaporization mechanism is the same for all three materials. This would imply that the much lower Cr vaporization rate for the Co-coated steel is due to the significantly lower activity of the Cr in the outermost surface oxide than in the outermost surface oxide of the uncoated material.

6.3 Self-healing mechanism of Co-coated and mechanically deformed interconnect steels

The interconnect material must be mechanically deformed to allow for gas distribution. When the 600 nm Co-coated Crofer 22 APU material was pressed into a real interconnect shape cracks within the coating were formed (Figure 6.3.1).
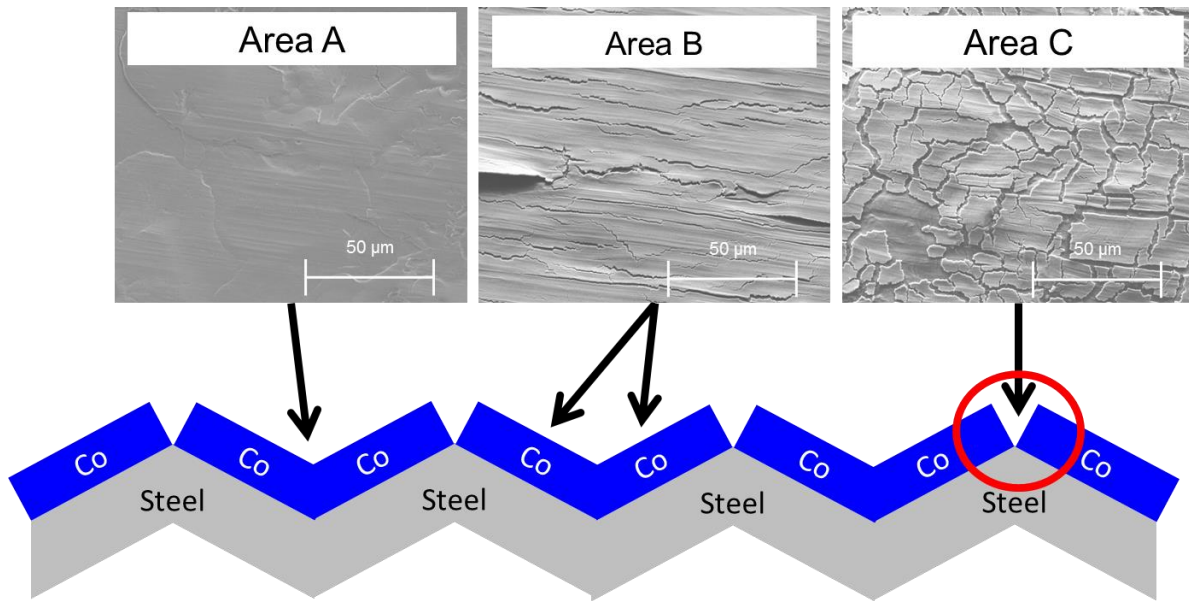
Figure 6.3.1. SEM images from different areas along the surface of the pre-coated material after being pressed into a real interconnect shape.

The extent of deformation varied over the interconnect surface and in some areas were cracks in the µm-range observed. All images shown hereinafter will be from the most severely deformed area (Area C). To investigate if the crack formation would increase high temperature oxidation and Cr vaporization the following four materials were studied (1) uncoated and undeformed, (2) Co-coated and undeformed, (3) deformed and subsequently coated (post-coated) and (4) pre-coated and subsequently deformed (Figure 4.1.1).

All Co-coated materials show a rapid gain in mass within the first minutes of exposure (Figure 6.3.2) which corresponds to the oxidation of the 600 nm Co-coating [25]. Furthermore, all three coated materials showed very similar mass gain behaviour which indicates that the mechanical deformation process did not influence oxidation behaviour up to 336 h.
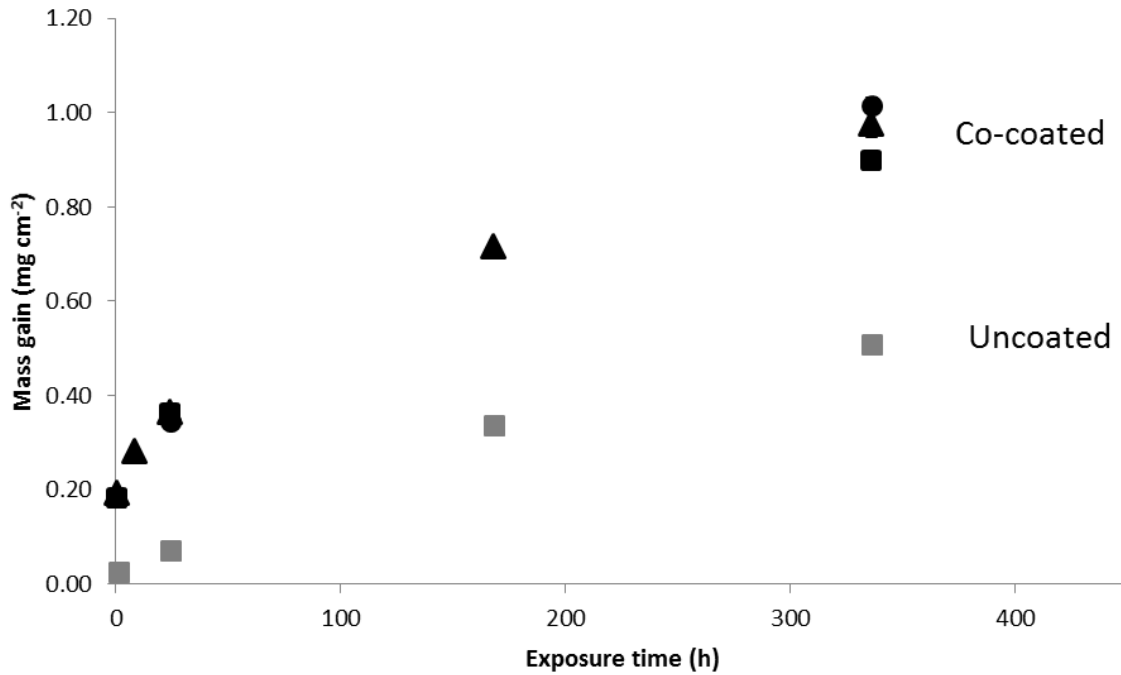
Figure 6.3.2: Mass gain as a function of time at 850 °C in air-3% H_2O (6000 sml min^{-1}). Uncoated undeformed (grey squares); coated undeformed (black squares); post-coated (black dots) and pre-coated (black triangles).

The amount of vaporized Cr was significantly less when the steel Crofer 22 APU was coated with 600 nm Co (Figure 6.3.3). Furthermore, pre-coating the steel, and pressing it into the interconnect shape did not increase Cr vaporization, since all coated materials vaporized approximately 90% less Cr than the uncoated material, which is in good agreement with earlier studies on similar ferritic stainless steels coated with ~600 nm Co [25, 29].
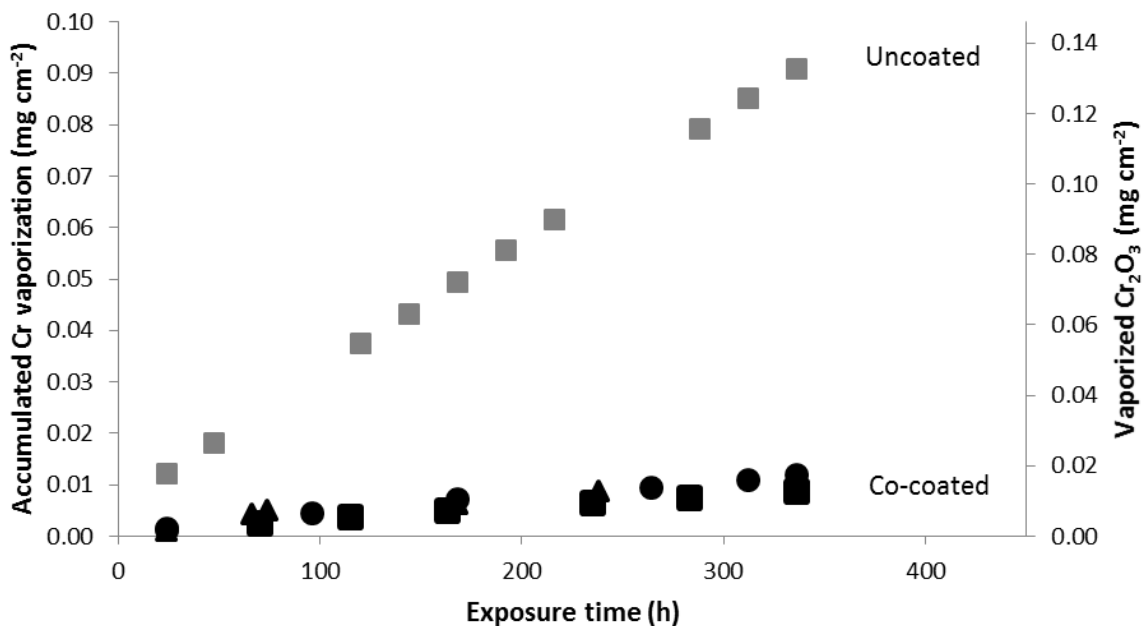
Figure 6.3.3: Accumulated Cr vaporization as a function of time at 850 °C in air-3% H_2O (6000 sml min^{-1}). Uncoated undeformed (grey squares); Coated undeformed (black squares); Post-coated (black dots) and Pre-coated (black triangles).

During exposure at high temperature, a Co and Mn rich oxide was formed within the cracked area. This "healing" of the oxide scale is most probably the reason no increase in Cr vaporization caused by the mechanical deformation process could be observed. After six minutes of exposure, the Co-coating had been turned into a Co-rich oxide [25] (Figure 6.3.4). The oxidation of the Co-coating is associated with a volume expansion (approximately the twice volume). This may have closed some of the smaller cracks; however, most of the cracks remain.
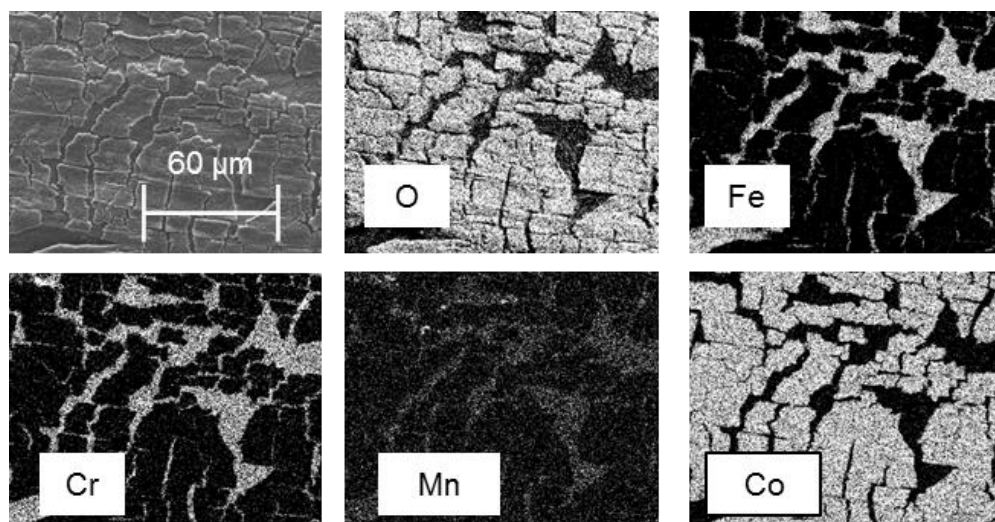
Figure 6.3.4: SEM image and EDX elemental maps for the mechanically deformed Crofer 22 APU + 600 nm Co (pre-coated) after 6 minutes of exposure in air containing 3% H_2O (6000 sml min^{-1}).

After 8 h of exposure (Figure 6.3.5), the cracked areas had become enriched in Mn, which suggests the formation of a $(Cr,Mn)_3O_4$ top layer, as observed by Sachitanand et al. [56] for uncoated Crofer APU in the same exposure environment.
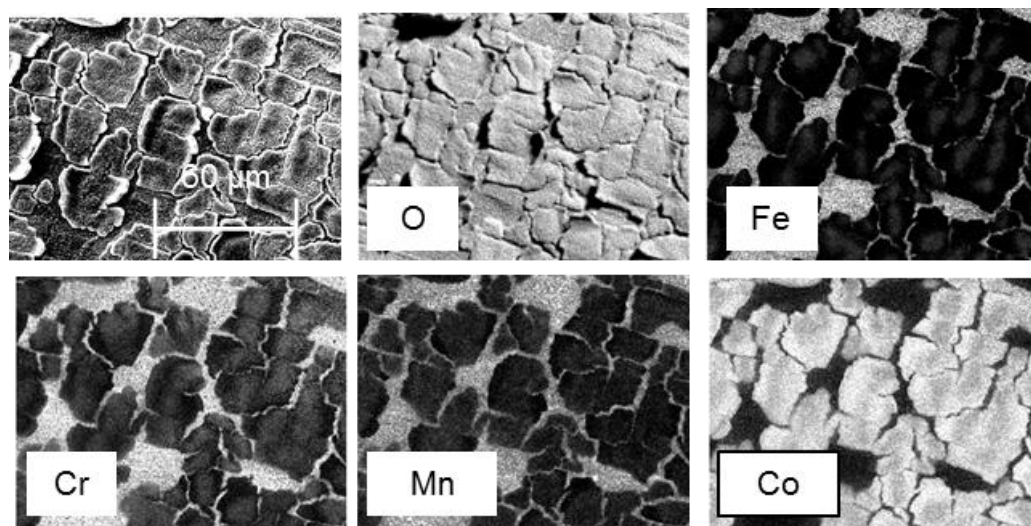
Figure 6.3.5: SEM image and EDX elemental maps for the mechanically deformed Crofer 22 APU + 600 nm Co (pre-coated) after 8 h of exposure in air containing 3% H_2O (6000 sml min^{-1}).

With continued exposure time a more homogenously distributed Cr, Mn and Co EDX signal is observed (Figure 6.3.6). The cracked areas remain rich in Mn after 24 h however, Co can partly be found within the cracked areas after 24 h. EDX mapping of a thin lamella from the sample exposed for 24 h (Figure 6.3.7) shows that the whole surface, including the cracked area, is covered with Co-oxide after only 24 h.
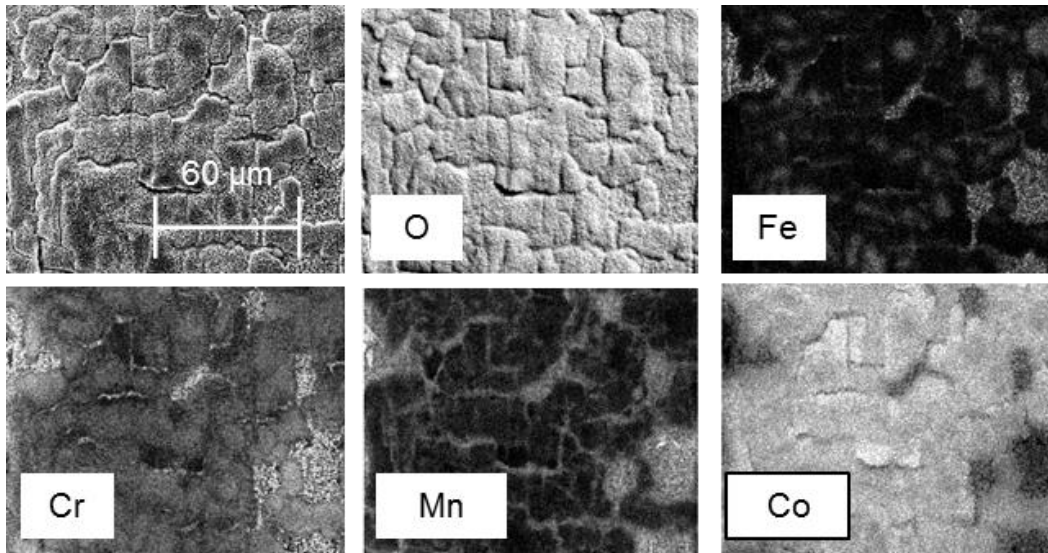
Figure 6.3.6: SEM image and EDX elemental maps for the mechanically deformed Crofer 22 APU + 600 nm Co (pre-coated) after 24 h of exposure in air containing 3% H_2O (6000 sml min^{-1}).
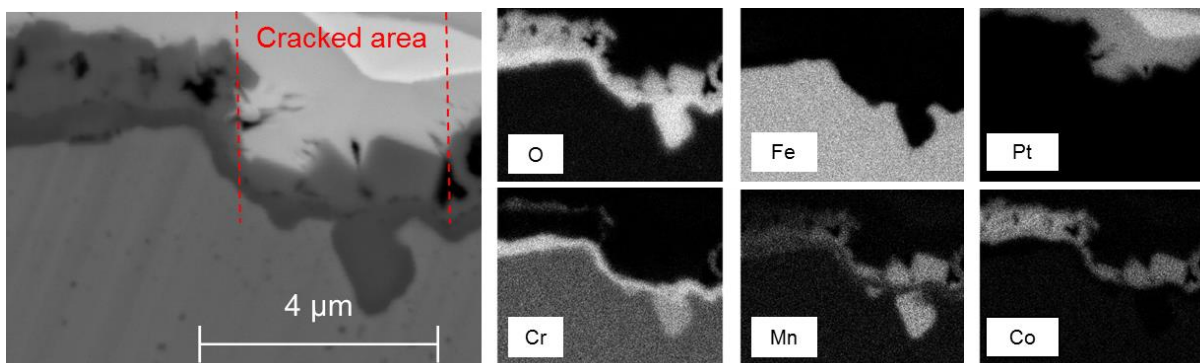
Figure 6.3.7: SEM image and EDX elemental maps of a thin lamella cut out by FIB milling from the mechanically deformed Crofer 22 APU + 600 nm Co (pre-coated) after 24 h of exposure in air containing 3% H_2O (6000 sml min^{-1}).

The fact that a large fraction of the surface within the cracked area was covered with a thin Co-rich oxide after only 24 h explains why no increase in Cr vaporization was observed during this time period. The morphology of the Co-oxide within the cracked area; however, differed significantly from the rest of the Co-oxide. The Co-oxide corresponding to the metallic Co coating before exposure was approximately 1-2 µm thick and contained large pores. The formation of rather large pores in thin metallic Co-coatings, probably as an effect of the fast oxidation of the Co-coating, has been observed earlier [25]. Since this Co_3O_4 was rather thick, it did not become enriched in Mn within 24 h of exposure. In contrast, the Co-oxide within the cracked area did not contain pores and was much richer in Mn. The thickness of the Co-oxide

within the cracked area varied significantly. This oxide consisted of a very thin continuous layer as well as a few large cubic crystals. The thin continuous $(Co,Mn)_3O_4$ layer was probably a thin $(Cr,Mn)_3O_4$ top layer, initially, which was then transformed into a $(Co,Mn)_3O_4$ top layer by means of solid state interdiffusion and/or surface diffusion. The large cubic $(Co,Mn)_3O_4$ crystals however, probably grew on the surface due to the diffusion of Co along the surface (surface and/or solid state interdiffusion) and the outward diffusion of Mn from the steel. With continued exposure time, all signs of cracks disappear (Figure 6.3.8). After 336 h of exposure the surface oxide had become homogenously rich in both Co and Mn (Figures 6.3.8 and 6.3.9). The growth of large $(Co,Mn)_3O_4$ crystals within the cracked area would explain why no signs of cracks could be observed after 336 h.
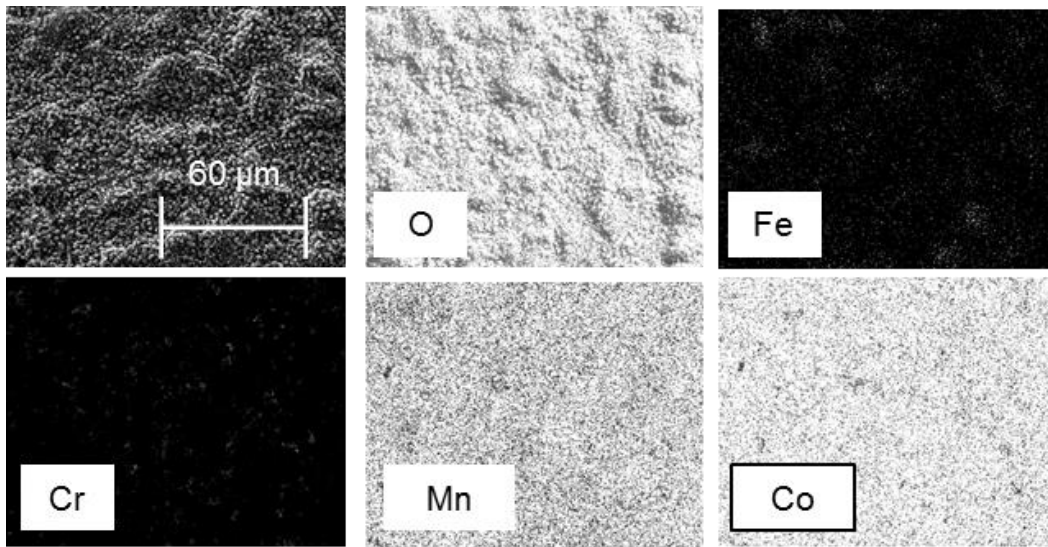
Figure 6.3.8: SEM image and EDX elemental maps for the mechanically deformed Crofer 22 APU + 600 nm Co (pre-coated) after 336 h of exposure in air containing 3% H_2O (6000 sml min^{-1}).
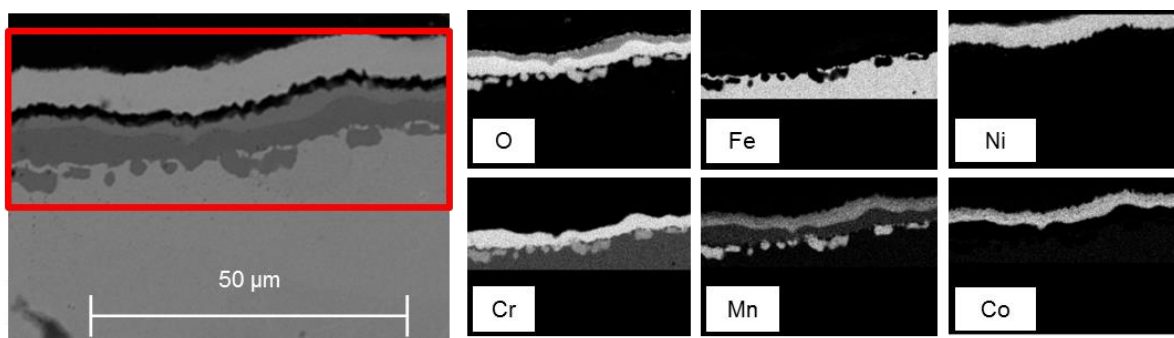
Figure 6.3.9: SEM image and EDX elemental maps of a cross section of the mechanically deformed Crofer 22 APU + 600 nm Co (pre-coated) after 336 h of exposure in air containing 3% H_2O (6000 sml min^{-1}).

The findings of this study indicate that pre-coated interconnect material can be utilized in an SOFC. The large cracks formed by the mechanical deformation process when a pre-coated material is pressed into an interconnect shape, can heal upon exposure at elevated temperatures.

6.4   Ce/Co coating (pre-coated)

To improve oxidation resistance, an additional layer of Ce was added between the steel and the 600 nm Co coating.
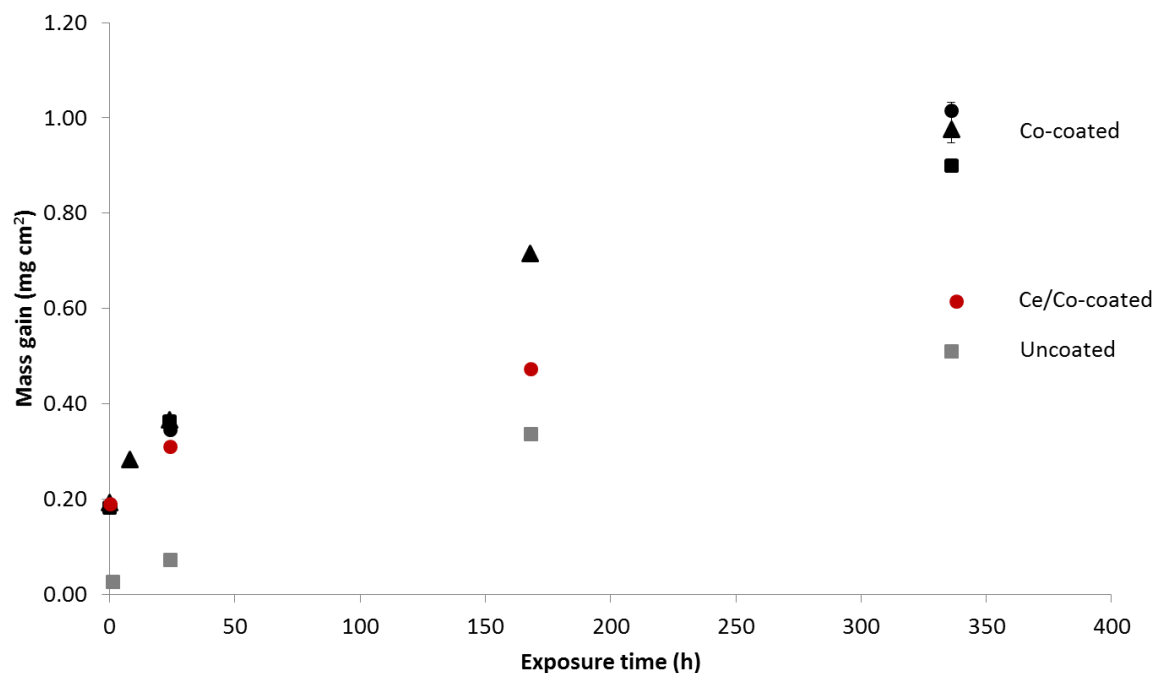
Figure 6.4.1: Mass gain as a function of time at 850 °C in air-3% H_2O (6000 sml min^{-1}) shown in Figure 6.3.1 including the pre-coated 10 nm Ce + 600 nm Co-coated material (red dots). Uncoated undeformed (grey squares); coated undeformed (black squares); post-coated (black dots) and pre-coated (black triangles).

The Ce/Co-coated material showed the same initial rapid mass gain associated with the oxidation of the Co-coating (Figure 6.4.1). However, with longer exposure time, the Ce/Co-coated material gained significantly less mass than the Co-coated (and the uncoated) material. This shows that adding a thin layer of 10 nm Ce to the Co-coated material effectively improves the oxidation resistance of the steel Crofer 22 APU.

The addition of a Ce layer between the steel and the Co-coating does not hinder the self-healing effect of the Co-coating (Figure 6.4.2).
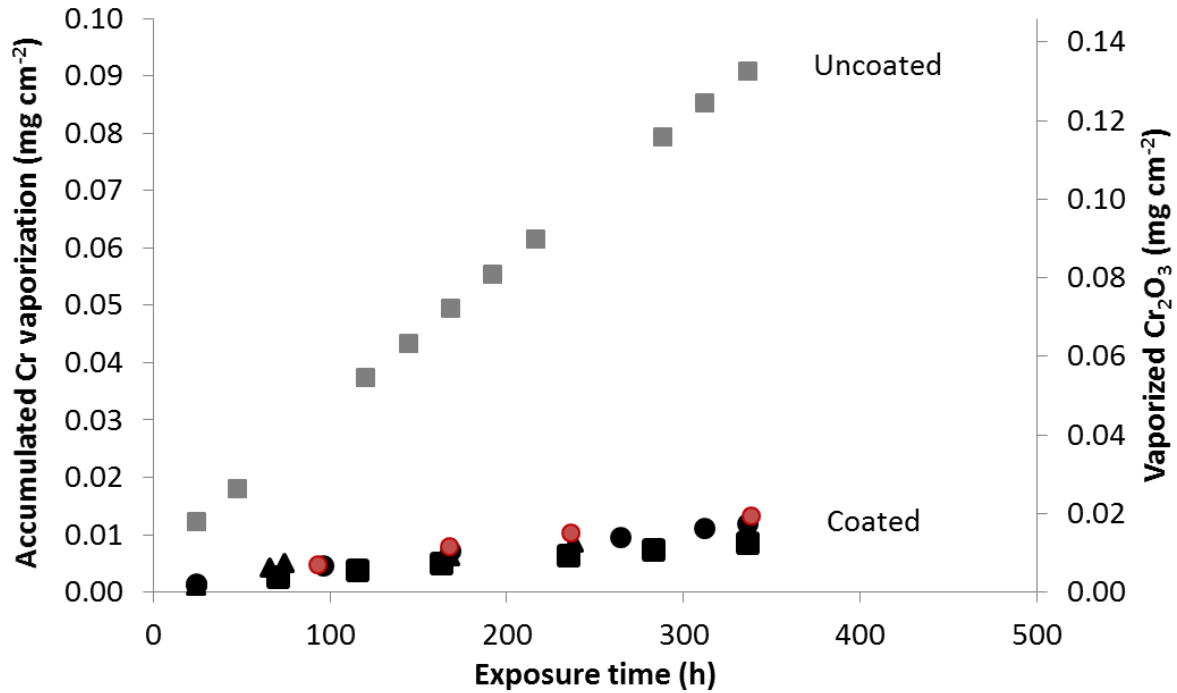
Figure 6.4.2: Accumulated Cr vaporization as a function of time at 850 °C in air-3% H_2O (6000 sml min^{-1}) shown in Figure 6.3.2 including the Ce/Co-coated material (red dots).

6.5 Electrical characterization of Ce/Co-coated Sanergy HT

In the previous section it was shown that a 10 nm thin layer of Ce significantly reduced the mass gain of the ferritic stainless steel Crofer 22 APU coated with 600 nm Co (Figure 6.4.2). Other published works on undeformed materials have also shown the positive effect of thin Ce coatings [27, 29, 30, 72]. However, decreasing the oxidation rate is only beneficial in an SOFC as long as electrical resistance does not increase. For this reason, the ferritic stainless steel Sanergy HT was coated with Ce/Co and exposed for up to 3000 h at 850 °C in an air 3% H_2O environment. Co-coated and uncoated materials were also exposed for comparison. Area Specific Resistance (ASR) measurements were carried out on samples exposed for 1000, 2000 and 3000 h
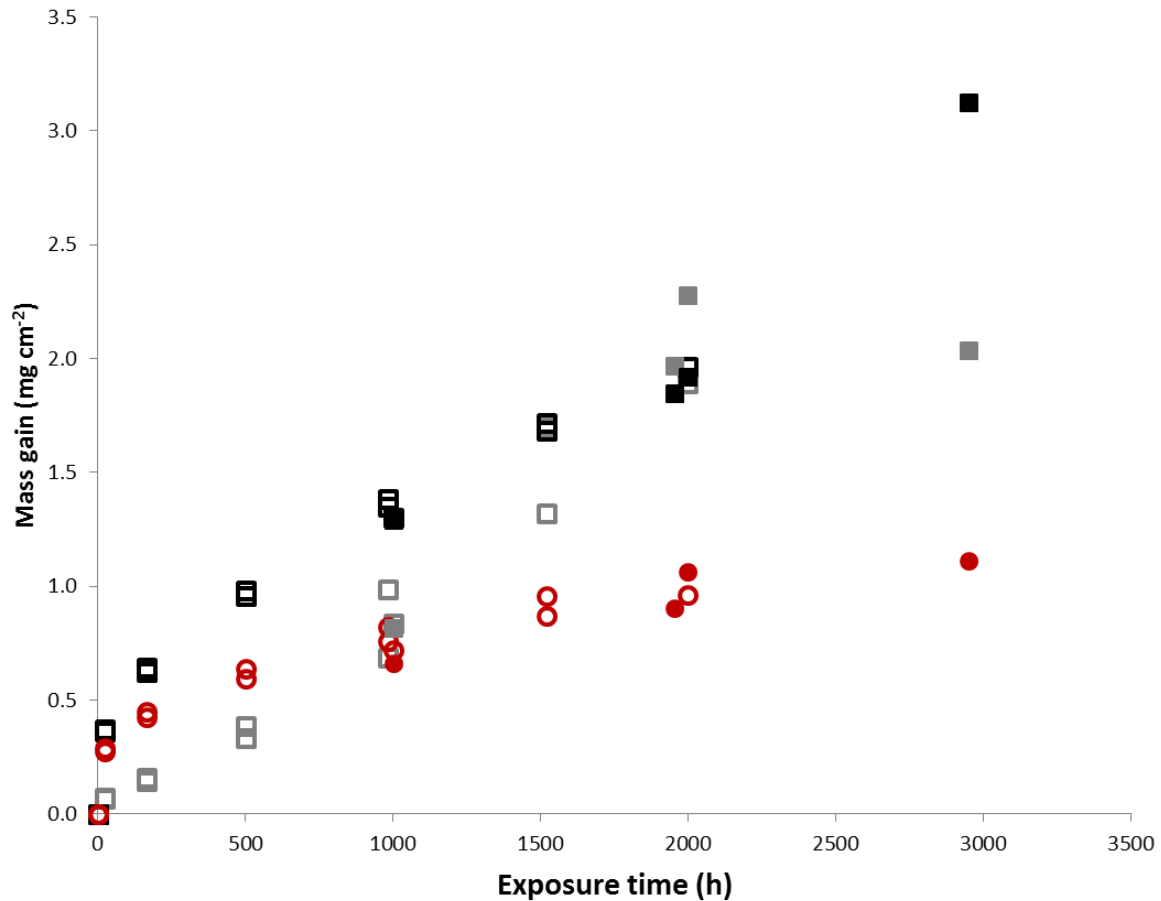
Figure 6.5.1: Mass gain as a function of time at 850 °C in air-3% H_2O (6000 sml min^{-1}). Uncoated (grey squares); Co-coated (black squares) and Ce/Co-coated (red dots). Each exposure (total of 2) initially contained six samples (two per material type). The exposure was interrupted at regular intervals and the samples were weighed to follow mass gain over time (empty symbols). After approximately 1000, 2000 and 3000 h, samples were removed for ASR characterization (filled symbols).

The two coated materials showed a rapid gain in mass initially, corresponding to the oxidation of the Co-coating [25] (Figure 6.5.1). After this rapid initial increase in mass, the Ce/Co-coated material showed a much lower mass gain rate than both the Co- and the uncoated material. Furthermore, the additional 10 nm Ce layer did not only decreased mass gain, but also significantly reduced area-specific resistance (Figure 6.5.2). For all measured exposure times (1000 – 3000 h) the Ce/Co-coated material showed the lowest ASR values and the uncoated material showed the highest.
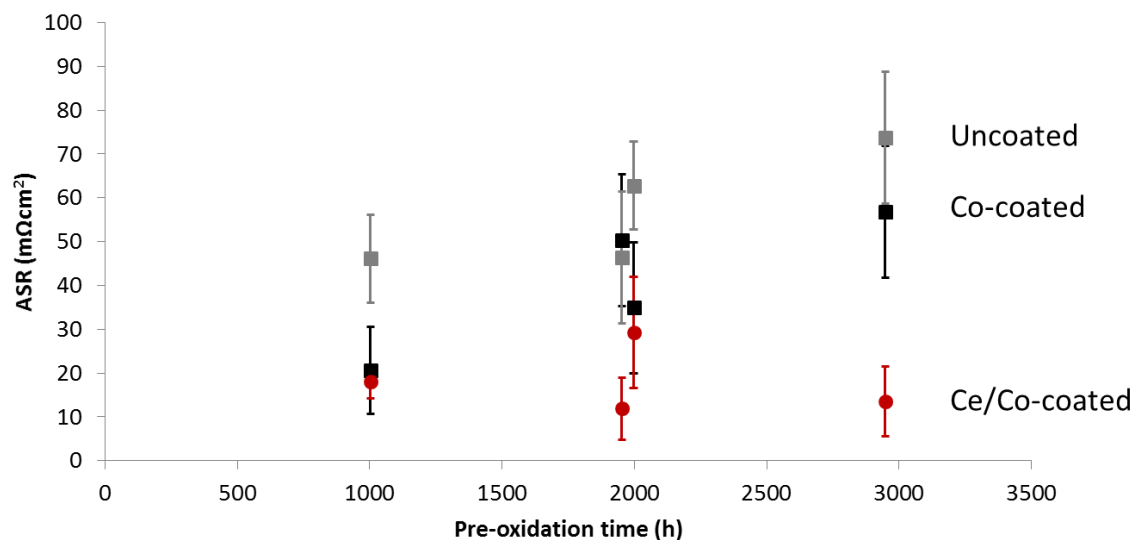
Figure 6.5.2: ASR values of pre-exposed samples (filled symbols in Figure 6.5.1) at 850 °C in air. Uncoated (grey squares); Co-coated (black squares) and Ce/Co-coated (red dots).

The thickness of the inner Cr_2O_3 layer was approximately the same for the Co- and the uncoated material which would explain why these two materials showed a similar increase in ASR value with time (Figure 6.5.3). The $(Co,Mn)_3O_4$ top layer on the Co-coated sample can be expected to conduct much better than the $(Cr,Mn)_3O_4$ top layer on the uncoated material [73]. This is assumed be the main reason for the somewhat lower ASR values for the Co-coated material than for the uncoated material. The Ce/Co-coated material, on the other hand, had formed a much thinner Cr_2O_3 layer than the two other materials. It is, therefore, proposed that the significantly lower ASR values for the Ce/Co-coated material are mainly due to the Cr_2O_3 scale for this material, which was thinner than for the Co-coated and the uncoated material.
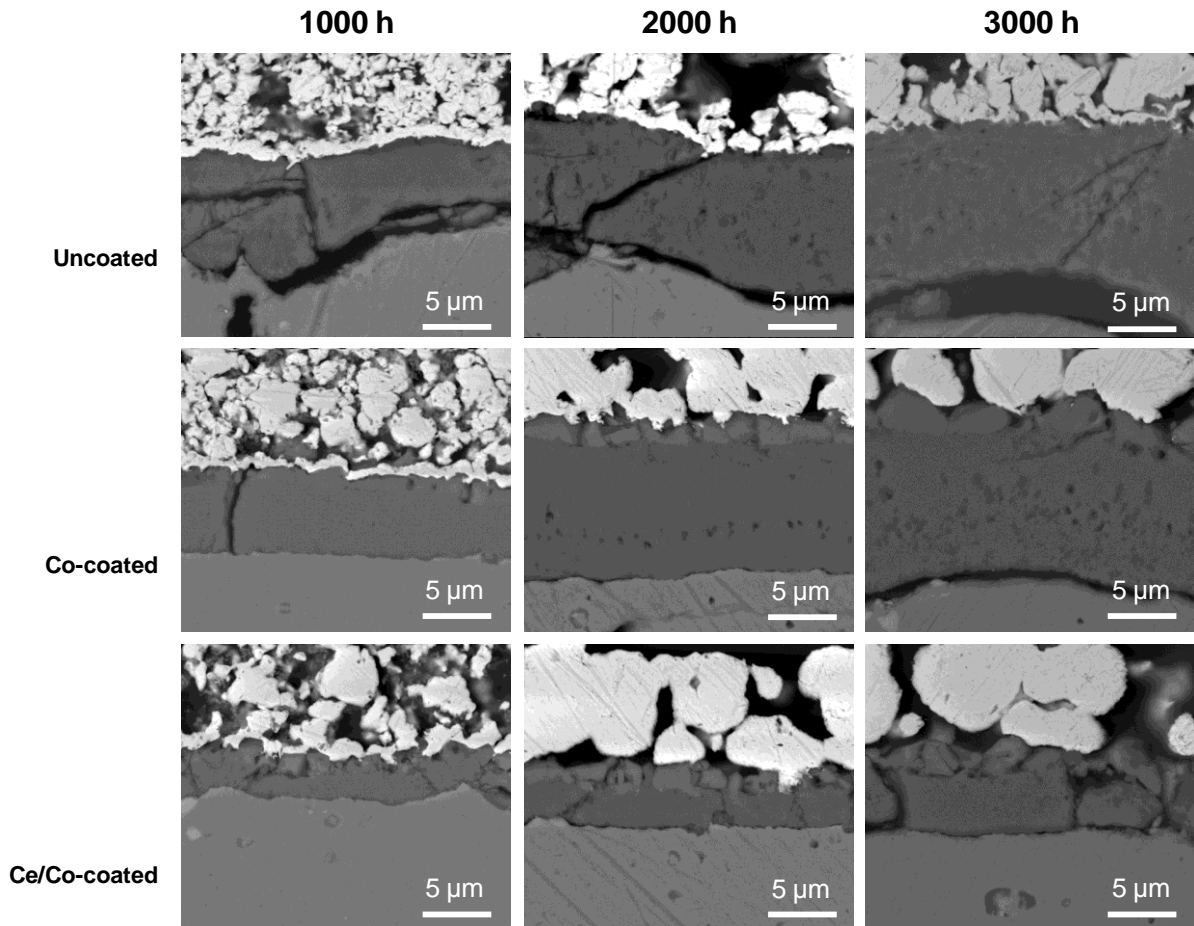
Figure 6.5.3: SEM (Backscattered) cross section images of the samples used for ASR measurements in Figure 6.5.2. Layers from top to bottom: Pt current collector, spinel top layer, Cr_2O_3 sub layer and the steel substrate.

7. Summary and outlook

The findings presented in this thesis address the two most common degradation mechanisms associated with the use of ferritic stainless steels as the interconnect material in SOFCs; Cr vaporization and oxide scale growth.

It was found that temperature has a significantly greater effect on oxide scale growth than Cr vaporization. As the temperature was decreased from 850 to 750 and 650 °C, paralinear mass gain behaviour was observed due to the high rate of Cr vaporization in comparison to the rate of oxide scale growth. To ensure the stable, long-term performance of an SOFC stack, high quality coatings that inhibit Cr vaporization are necessary, even if the operating temperature is decreased to temperatures as low as 650 °C.

By applying a metallic Co coating that is ~600 nm thick, the rate of Cr vaporization could be reduced by almost 90 %. Cr vaporization measurements at different temperatures were carried out to calculate the activation energy value for Cr vaporization from Cr_2O_3, uncoated and Co-coated steel. Findings revealed that all three materials showed similar activation energy values for Cr vaporization, which indicates that the beneficial effect of the Co-coating is not a direct effect of any change in mechanism. Instead, it is proposed that the much lower rate of Cr vaporization achieved with a Co-coating is due to the much lower Cr activity within the outermost oxide scale.

When Co-coated ferritic stainless steels are pressed into real interconnects, large cracks arise within the coating due to tensile deformation. It was found that the formation of these cracks; however, did not increase Cr vaporization. Due to fast Co diffusion, a top layer of $(Co,Mn)_3O_4$ was established within the cracked area after only 24 h of exposure. The $(Co,Mn)_3O_4$ layer within the cracked area grew thicker with continued exposure time, and after 336 h the surface of the pre-coated material was homogenously covered by an oxide rich in Co and Mn.

Furthermore, by applying a thin layer of 10 nm Ce between the steel and the Co coating corrosion resistance could be improved significantly without increasing Cr vaporization. Such a double-layered coating of Ce and Co not only improved the corrosion resistance of the steel, but also the electrical resistance of the steel was significantly reduced.

It has been shown that thin metallic Ce/Co coatings on ferritic stainless steels can significantly reduce the degradation associated with oxide scale growth and Cr vaporization. Large amounts of steel can be pre-coated in a cost-effective way without increasing Cr vaporization due to crack formation when the material is deformed to allow for gas distribution.

The results of this thesis have also shown that higher temperatures, as a method to accelerate corrosion, may lead to fundamental differences in chemical composition and morphology. Therefore, an important part of future research will be concentrated on lower temperatures. More fundamental research to understand the two degradation mechanisms, Cr vaporization and oxide scale growth, should be carried out. A better understanding of the Cr vaporization mechanism could help to develop new alternative coatings that reduce Cr vaporization. The beneficial effect of Ce is not fully understood and will be included in future research.

8. References

[1]   J. Larminie and A. Dicks, *Fuel Cell Systems Explained*. 2003: J. Wiley.

[2]   A. Kirubakaran, S. Jain, and R.K. Nema, *A review on fuel cell technologies and power electronic interface.* Renewable & Sustainable Energy Reviews, 2009. **13**(9): p. 2430-2440.

[3]   S.C. Singhal and K. Kendall, *High Temperature Solid Oxide Fuel Cells: Fundamentals, Design, and Applications*. 2003: Elsevier.

[4]   A.B. Stambouli and E. Traversa, *Solid oxide fuel cells (SOFCs): a review of an environmentally clean and efficient source of energy.* Renewable & Sustainable Energy Reviews, 2002. **6**(5): p. 433-455.

[5]   M. Powell, K. Meinhardt, V. Sprenkle, L. Chick, and G. McVay, *Demonstration of a highly efficient solid oxide fuel cell power system using adiabatic steam reforming and anode gas recirculation.* Journal of Power Sources, 2012. **205**: p. 377-384.

[6]   S.P.S. Badwal, S. Giddey, C. Munnings, and A. Kulkarni, *Review of Progress in High Temperature Solid Oxide Fuel Cells.* Journal of the Australian Ceramic Society, 2014. **50**(1): p. 23-37.

[7]   E.D. Wachsman and K.T. Lee, *Lowering the Temperature of Solid Oxide Fuel Cells.* Science, 2011. **334**(6058): p. 935-939.

[8]   J.W. Fergus, *Metallic interconnects for solid oxide fuel cells.* Materials Science and Engineering a-Structural Materials Properties Microstructure and Processing, 2005. **397**(1-2): p. 271-283.

[9]   W.Z. Zhu and S.C. Deevi, *Opportunity of metallic interconnects for solid oxide fuel cells: a status on contact resistance.* Materials Research Bulletin, 2003. **38**(6): p. 957-972.

[10]   B.B. Ebbinghaus, *Thermodynamics of Gas-Phase Chromium Species - the Chromium Oxides, the Chromium Oxyhydroxides, and Volatility Calculations in Waste Incineration Processes.* Combustion and Flame, 1993. **93**(1-2): p. 119-137.

[11]   C. Gindorf, L. Singheiser, and K. Hilpert, *Vaporisation of chromia in humid air.* Journal of Physics and Chemistry of Solids, 2005. **66**(2-4): p. 384-387.

[12]   K. Hilpert, D. Das, M. Miller, D.H. Peck, and R. Weiss, *Chromium vapor species over solid oxide fuel cell interconnect materials and their potential for degradation processes.* Journal of the Electrochemical Society, 1996. **143**(11): p. 3642-3647.

[13]   E.J. Opila, et al., *Theoretical and experimental investigation of the thermochemistry of CrO2(OH)(2)(g).* Journal of Physical Chemistry A, 2007. **111**(10): p. 1971-1980.

[14]   S.P.S. Badwal, R. Deller, K. Foger, Y. Ramprakash, and J.P. Zhang, *Interaction between chromia forming alloy interconnects and air electrode of solid oxide fuel cells.* Solid State Ionics, 1997. **99**(3-4): p. 297-310.

[15]   J.W. Fergus, *Effect of cathode and electrolyte transport properties on chromium poisoning in solid oxide fuel cells.* International Journal of Hydrogen Energy, 2007. **32**(16): p. 3664-3671.

[16]   S.P. Simner, M.D. Anderson, G.G. Xia, Z. Yang, L.R. Pederson, and J.W. Stevenson, *SOFC performance with Fe-Cr-Mn alloy interconnect.* Journal of the Electrochemical Society, 2005. **152**(4): p. A740-A745.

[17]   M.C. Tucker, H. Kurokawa, C.P. Jacobson, L.C. De Jonghe, and S.J. Visco, *A fundamental study of chromium deposition on solid oxide fuel cell cathode materials.* Journal of Power Sources, 2006. **160**(1): p. 130-138.

[18]   S.R. Akanda, N.J. Kidner, and M.E. Walter, *Spinel coatings on metallic interconnects: Effect of reduction heat treatment on performance.* Surface & Coatings Technology, 2014. **253**: p. 255-260.

[19]   E. Alvarez, A. Meier, K.S. Weil, and Z.G. Yang, *Oxidation Kinetics of Manganese Cobaltite Spinel Protection Layers on Sanergy HT for Solid Oxide Fuel Cell Interconnect Applications.* International Journal of Applied Ceramic Technology, 2011. **8**(1): p. 33-41.

[20]   P.E. Gannon, et al., *Enabling inexpensive metallic alloys as SOFC interconnects: An investigation into hybrid coating technologies to deposit nanocomposite functional coatings on ferritic stainless steels.* International Journal of Hydrogen Energy, 2007. **32**(16): p. 3672-3681.

[21]   Y.Z. Hu, C.X. Li, G.J. Yang, and C.J. Li, *Evolution of microstructure during annealing of Mn1.5Co1.5O4 spinel coatings deposited by atmospheric plasma spray.* International Journal of Hydrogen Energy, 2014. **39**(25): p. 13844-13851.

[22]   N.J. Magdefrau, L. Chen, E.Y. Sun, and M. Aindow, *The effect of Mn1.5Co1.5O4 coatings on the development of near surface microstructure for Haynes 230 oxidized at 800 degrees C in air.* Surface & Coatings Technology, 2014. **242**: p. 109-117.

[23]   B.K. Park, et al., *Cu- and Ni-doped Mn1.5Co1.5O4 spinel coatings on metallic interconnects for solid oxide fuel cells.* International Journal of Hydrogen Energy, 2013. **38**(27): p. 12043-12050.

[24]   R. Trebbels, T. Markus, and L. Singheiser, *Investigation of Chromium Vaporization from Interconnector Steels with Spinel Coatings.* Journal of the Electrochemical Society, 2010. **157**(4): p. B490-B495.

[25]   J. Froitzheim, S. Canovic, M. Nikumaa, R. Sachitanand, L.G. Johansson, and J.E. Svensson, *Long term study of Cr evaporation and high temperature corrosion behaviour of Co coated ferritic steel for solid oxide fuel cell interconnects.* Journal of Power Sources, 2012. **220**: p. 217-227.

[26]   J. Froitzheim, et al., *Nano Coated Interconnects for SOFC (NaCoSOFC).* Solid Oxide Fuel Cells 13 (Sofc-Xiii), 2013. **57**(1): p. 2187-2193.

[27]   J. Froitzheim and J.E. Svensson, *Multifunctional Nano-Coatings for SOFC Interconnects.* Solid Oxide Fuel Cells 12 (Sofc Xii), 2011. **35**(1): p. 2503-2508.

[28]   J. Froitzheim, H. Ravash, E. Larsson, L.G. Johansson, and J.E. Svensson, *Investigation of Chromium Volatilization from FeCr Interconnects by a Denuder Technique.* Journal of the Electrochemical Society, 2010. **157**(9): p. B1295-B1300.

[29]   J.G. Grolig, J. Froitzheim, and J.E. Svensson, *Coated stainless steel 441 as interconnect material for solid oxide fuel cells: Oxidation performance and chromium evaporation.* Journal of Power Sources, 2014. **248**: p. 1007-1013.

[30]   S. Canovic, et al., *Oxidation of Co- and Ce-nanocoated FeCr steels: A microstructural investigation.* Surface and Coatings Technology, 2013. **215**(0): p. 62-74.

[31]   B.C.H. Steele and A. Heinzel, *Materials for fuel-cell technologies.* Nature, 2001. **414**(6861): p. 345-352.

[32]   J.G. Grolig, *Coated Ferritic Stainless Steels as Interconnects in Solid Oxide Fuel Cells.* 2013.

[33]   N. Shaigan, W. Qu, D.G. Ivey, and W.X. Chen, *A review of recent progress in coatings, surface modifications and alloy developments for solid oxide fuel cell ferritic stainless steel interconnects.* Journal of Power Sources, 2010. **195**(6): p. 1529-1542.

[34]   P. Kofstad, *High Temperature Corrosion.* Elsevier Applied Science, 1988.

[35]   D.J. Young, *High Temperature Oxidation and Corrosion of Metals*. 2008: Elsevier.

[36]   H.J.T. Ellingham, *Reducibility of oxides and sulphides in metallurgical processes.* Journal of the Society of Chemical Industry, 1944. **63**(5): p. 125-160.

[37]   T. Jonsson, B. Pujilaksono, A. Fuchs, J.E. Svensson, L.G. Johansson, and M. Halvarsson, *The influence of H(2)O on iron oxidation at 600 degrees C: A microstructural study.* High Temperature Corrosion and Protection of Materials 7, Pts 1 and 2, 2008. **595-598**: p. 1005-1012.

[38]   N. Birks, G.H. Meier, and F.S. Pettit, *Introduction to the high temperature oxidation of metals*. 2006: Cambridge University Press.

[39]   M. Hasegawa, *Chapter 3.3 – Ellingham Diagram.* Treatise on Process Metallurgy: Process Fundamentals, 2014. **1**: p. 507–516.

[40]   A.R. West, *Basic solid state chemistry*. 1999: John Wiley & Sons.

[41]   H. Mehrer, *Diffusion in Solids: Fundamentals, Methods, Materials, Diffusion-Controlled Processes*. 2007: Springer.

[42]   C.S. Tedmon, *Effect of Oxide Volatilization on Oxidation Kinetics of Cr and Fe-Cr Alloys.* Journal of the Electrochemical Society, 1966. **113**(8): p. 766-&.

[43]   E. Konysheva, et al., *Chromium poisoning of perovskite cathodes by the ODS alloy Cr5Fe1Y(2)O(3) and the high chromium ferritic steel Crofer22APU.* Journal of the Electrochemical Society, 2006. **153**(4): p. A765-A773.

[44] H. Kurokawa, C.P. Jacobson, L.C. DeJonghe, and S.J. Visco, *Chromium vaporization of bare and of coated iron-chromium alloys at 1073 K.* Solid State Ionics, 2007. **178**(3-4): p. 287-296.

[45] G.Y. Lau, M.C. Tucker, C.P. Jacobson, S.J. Visco, S.H. Gleixner, and L.C. DeJonghe, *Chromium transport by solid state diffusion on solid oxide fuel cell cathode.* Journal of Power Sources, 2010. **195**(22): p. 7540-7547.

[46] M. Stanislowski, E. Wessel, K. Hilpert, T. Markus, and L. Singheiser, *Chromium vaporization from high-temperature alloys I. Chromia-forming steels and the influence of outer oxide layers.* Journal of the Electrochemical Society, 2007. **154**(4): p. A295-A306.

[47] D.E. Alman and P.D. Jablonski, *Effect of minor elements and a Ce surface treatment on the oxidation behavior of an Fe-22Cr-0.5Mn (Crofer 22 APU) ferritic stainless steel.* International Journal of Hydrogen Energy, 2007. **32**(16): p. 3743-3753.

[48] J. Quadakkers and L. Singheiser, *Practical aspects of the reactive element effect.* High Temperature Corrosion and Protection of Materials 5, Pts 1 and 2, 2001. **369-3**: p. 77-92.

[49] B. Pint. *Progress in understanding the reactive element effect since the Whittle and Stringer literature review*. in *Proceedings of the John Stringer Symposium. Edited by PF Tortorelli and PY Hou. ASM, Materials Park, OH*. 2003. Citeseer.

[50] E.A. Polman, T. Fransen, and P.J. Gellings, *The Reactive Element Effect - Ionic Processes of Grain-Boundary Segregation and Diffusion in Chromium-Oxide Scales.* Journal of Physics-Condensed Matter, 1989. **1**(28): p. 4497-4510.

[51] C.M. Cotell, G.J. Yurek, R.J. Hussey, D.F. Mitchell, and M.J. Graham, *The Influence of Implanted Yttrium on the Mechanism of Growth of Cr2o3 on Cr.* Journal of the Electrochemical Society, 1987. **134**(7): p. 1871-1872.

[52] B.A. Pint, *Experimental observations in support of the dynamic-segregation theory to explain the reactive-element effect.* Oxidation of Metals, 1996. **45**(1-2): p. 1-37.

[53] R.W. Jackson, et al., *Analysis of the Reactive Element Effect on the Oxidation of Ceria Doped Nickel.* Oxidation of Metals, 2012. **78**(3-4): p. 197-210.

[54] A. Balland, P. Gannon, M. Deibert, S. Chevalier, G. Caboche, and S. Fontana, *Investigation of La2O3 and/or (Co,Mn)(3)O-4 deposits on Crofer22APU for the SOFC interconnect application.* Surface & Coatings Technology, 2009. **203**(20-21): p. 3291-3296.

[55] S. Fontana, S. Chevalier, and G. Caboche, *Metallic Interconnects for Solid Oxide Fuel Cell: Performance of Reactive Element Oxide Coating During 10, 20 and 30 Months Exposure.* Oxidation of Metals, 2012. **78**(5-6): p. 307-328.

[56] R. Sachitanand, M. Sattari, J.E. Svensson, and J. Froitzheim, *Evaluation of the oxidation and Cr evaporation properties of selected FeCr alloys used as SOFC interconnects.* International Journal of Hydrogen Energy, 2013. **38**(35): p. 15328-15334.

[57] M. Stanislowski, et al., *Reduction of chromium vaporization from SOFC interconnectors by highly effective coatings.* Journal of Power Sources, 2007. **164**(2): p. 578-589.

[58] A. Harthøj, T. Holt, and P. Møller, *Oxidation behaviour and electrical properties of cobalt/cerium oxide composite coatings for solid oxide fuel cell interconnects.* Journal of Power Sources, 2015. **281**(0): p. 227-237.

[59] M. Dewar, *Characterization and Evaluation of Aged 20Cr32Ni1Nb Stainless Steels.* 2013.

[60] K.L. Scrivener, *Backscattered electron imaging of cementitious microstructures: understanding and quantification.* Cement & Concrete Composites, 2004. **26**(8): p. 935-945.

[61] P. Huczkowski, et al., *Effect of component thickness on lifetime and oxidation rate of chromia forming ferritic steels in low and high pO(2) environments.* Materials at High Temperatures, 2005. **22**(3-4): p. 253-262.

[62] I.H. Jung, *Critical evaluation and thermodynamic modeling of the Mn-Cr-O system for the oxidation of SOFC interconnect.* Solid State Ionics, 2006. **177**(7-8): p. 765-777.

[63] T. Brylewski, J. Dabek, and K. Przybylski, *Oxidation kinetics study of the iron-based steel for solid oxide fuel cell application.* Journal of Thermal Analysis and Calorimetry, 2004. **77**(1): p. 207-216.

[64] H. Hindam and D.P. Whittle, *Microstructure, Adhesion and Growth-Kinetics of Protective Scales on Metals and Alloys.* Oxidation of Metals, 1982. **18**(5-6): p. 245-284.

[65] E.A. Gulbransen and K.F. Andrew, *Kinetics of the Oxidation of Chromium.* Journal of the Electrochemical Society, 1957. **104**(6): p. 334-338.

[66] A.M. Huntz, et al., *Oxidation of AISI 304 and AISI 439 stainless steels.* Materials Science and Engineering a-Structural Materials Properties Microstructure and Processing, 2007. **447**(1-2): p. 266-276.

[67] A.C.S. Sabioni, et al., *Atmosphere dependence of oxidation kinetics of unstabilized and Nb-stabilized AISI 430 ferritic stainless steels in the temperature range 850-950 degrees C.* Materials at High Temperatures, 2010. **27**(2): p. 89-96.

[68] A.W.B. Skilbred and R. Haugsrud, *Sandvik Sanergy HT - A potential interconnect material for LaNbO4-based proton ceramic fuel cells.* Journal of Power Sources, 2012. **206**: p. 70-76.

[69] W.C. Hagel and A.U. Seybolt, *Cation Diffusion in Cr2o3.* Journal of the Electrochemical Society, 1961. **108**(12): p. 1146-1152.

[70] I. Panas, J.E. Svensson, H. Asteman, T.J.R. Johnson, and L.G. Johansson, *Chromic acid evaporation upon exposure of Cr2O3(S) to H2O(g) and O-2(g) - mechanism from first principles.* Chemical Physics Letters, 2004. **383**(5-6): p. 549-554.

[71] A. Harthøj, *Electroplating of Protective Coatings on Interconnects Used for Solid Oxide Fuel Cell Stacks*, in *Department of Mechanical Engineering*2014, Technical University of Denmark: Lyngby, Denmark.

[72] H.F. Windisch, J. Froitzheim, and J.E. Svensson, *Influence of Chromium Evaporation and Oxidation on Interconnect Steels at 650-850 degrees C.* Solid Oxide Fuel Cells 13 (Sofc-Xiii), 2013. **57**(1): p. 2225-2233.

[73] A. Petric and H. Ling, *Electrical conductivity and thermal expansion of spinels at elevated temperatures.* Journal of the American Ceramic Society, 2007. **90**(5): p. 1515-1520.